AIAA JOURNAL
Vol. 50, No. 3, March 2012

Effects of Surface Roughness on Separated and Transitional Flows over a Wing

Ying Zhou* and Z. J. Wang†
Iowa State University, Ames, Iowa 50011

DOI: 10.2514/1.J051237

Laminar separation bubbles are often found over the wing of micro air vehicles at low Reynolds numbers and strongly influence the lift, drag, and other aerodynamic performance parameters. A numerical investigation of passive separation control techniques using roughness bumps on a low-Reynolds-number wing is conducted in the present study. A high-order spectral difference unstructured-grid Navier–Stokes solver is employed in the simulations. The study of surface roughness on laminar separation and turbulent transition can provide insights into the design of future passive control devices on wings. The transitional flow with laminar separation bubble past a SD7003 rectangular wing with Reynolds number of 60,000 is used as the baseline (uncontrolled) case. In the controlled cases, roughness bumps are strategically placed near the leading edge of the wing for the purpose of improving aerodynamic performance in terms of the lift-to-drag ratio. The location, bump size, number of bumps, and angle of attack are varied to study the effects. The pressure drag forces in the controlled cases are found to be reduced significantly when the separation is reduced or avoided, resulting in much improved lift-over-drag ratio.

Nomenclature

C_D	=	drag coefficient
C_{Df}	=	drag coefficient contributed by friction
C_{Dp}	=	drag coefficient contributed by pressure
C_f	=	skin-friction coefficient
C_L	=	lift coefficient
C_p	=	pressure coefficient
c	=	chord length
$F, G, H,$ $\tilde{F}, \tilde{G}, \tilde{H}$	=	vector of fluxes in Cartesian coordinates and standard unstructured elements
$\tilde{F}^i, \tilde{F}^v$	=	inviscid and viscous vector of fluxes in standard unstructured elements
H_{EF}, L_{BD}, W_{AC}	=	height, length and width the of the roughness bump
$h_i, l_{i+1/2}$	=	coefficient of Lagrange polynomial interpolation at solution points and flux points
i, j, k	=	index of coordinates in x, y, z directions
J	=	Jacobian matrix
K	=	number of points in physical element
L/D	=	lift-to-drag ratio
M	=	Mach number
M_i	=	shape function in coordinate transformation
N_{bump}	=	number of roughness bumps
P_{Total}	=	normalized mean total pressure, $(\frac{1}{2}\rho U^2 + P)/\frac{1}{2}\rho_\infty U_\infty^2$
p	=	nondimensional pressure
$Q, \tilde{Q}$	=	vector of conservative variables in Cartesian coordinates and standard unstructured elements
Q_L, Q_R	=	vector of conservative variables from the two elements beside the interface
Re_c	=	Reynolds number based on chord length
s	=	wave speed of the disturbance in linear stability theory, $s = \omega/\alpha_r$
T	=	nondimensional temperature
TKE	=	normalized turbulent kinetic energy, $\frac{1}{2}(\bar{u}'^2 + \bar{v}'^2 + \bar{w}'^2)/U_\infty^2$
t	=	nondimensional time $t = t^*/(c/U_\infty)$
t^*	=	dimensional time
U_∞	=	freestream velocity
u, v, w	=	nondimensional velocity in x, y, z direction
u', v', w'	=	nondimensional velocity fluctuation in x, y, z direction
u_t, u_t'	=	nondimensional tangential velocity/ fluctuation, normal to the wall surface
x, y, z	=	nondimensional Cartesian coordinates
X_E	=	location of the roughness bump
X_s	=	solution points in spectral difference method
$X_{s+1/2}$	=	flux points in spectral difference method
α_r	=	wave number of the disturbances in x direction in linear stability theory
α_i	=	growth rate of the disturbances in linear stability theory
β	=	wave number of the disturbances in z direction in linear stability theory
$\Delta x^+, \Delta y^+, \Delta z^+$	=	cell size in wall units
δ_E	=	boundary-layer thickness at the location of bump in uncontrolled case
$\xi_x, \eta_x, \varsigma_x, \xi_y,$ $\eta_y, \varsigma_y, \xi_z, \eta_z, \varsigma_z$	=	metric coefficients of the coordinate transformation
ρ	=	nondimensional density
τ_{xy}	=	normalized Reynolds stress, $\overline{u'v'}/U_\infty^2$
ϕ	=	vector of primitive variables
Ω	=	computational spatial domain
ω	=	frequency of the disturbances in linear stability theory
$\lvert\nabla P\rvert$	=	magnitude of pressure gradient
∇Q	=	gradient of conservative variables

Presented as Paper 2011-736 at the 49th AIAA Aerospace Sciences Meeting, Orlando, FL, 4–7 January 2011; received 21 March 2011; revision received 15 July 2011; accepted for publication 19 August 2011.

*Ph.D. Student, Department of Aerospace Engineering and CFD Center. Student Member AIAA.

†Professor, Department of Aerospace Engineering and CFD Center. Associate Fellow AIAA.

I. Introduction

FLOW control, the technique to manipulate a flowfield to achieve a desired change, is of immense technological importance and is

thus pursued by many scientists and engineers in various areas of fluid mechanics field for many years. The configuration lift, drag, and L/D ratio are the principal considerations in the design and construction of air vehicles. The decrease in drag and increase in L/D ratio can increase the range and reduce the required thrust, which result in improved fuel economy. Low-Reynolds-number ($Re_c = 10^4 \sim 10^5$) flow has been of interest for many decades with the development of micro air vehicles. In the low-Reynolds-number flows over airfoils, the formation of a laminar separation bubble (LSB) has a dominant effect on the flowfield and usually causes high-pressure drag force on the airfoil. Reducing or avoiding the separation on the surfaces of the airfoils is one way of achieving reduced drag. Because of this, aerodynamicists and aircraft designers have pursued the objective of separation control for many decades.

Since laminar boundary layers are less resistible to the significant adverse pressure gradient, LSBs are widely found in the time-mean flowfield over the suction side of low-Reynolds-number airfoils at moderate incidences. At moderate angles of attack (AOA), the laminar flow detaches from the suction wing surface near the leading edge and a LSB is formed. After separation, vortex shedding due to the Kelvin–Helmholtz (K-H) instability is usually observed within the separation region. Thereafter, the separated laminar boundary layer rapidly transitions to turbulent flows and the turbulent boundary layer reattaches after the vortex breakdown.

Active flow control techniques have been widely adopted for the separation and transition control of flow over airfoils. Periodic air suction/blowing through a slot on the airfoil surface, which introduces momentum into the flowfield, might be the most popular means of active control. With properly chosen frequency and magnitude of the suction/blowing speed, the technique is often found to be effective in reducing the separation region and improving performance (e.g., [1]). Plasma actuators are applied as another technique of active flow control (e.g., [2]). However, active control techniques such as suction/blowing and plasma actuator usually require additional devices and power and are less applicable to the separation control over a micro air vehicle wing, which should be light and small. The passive means of flow control involves inert devices including changes to the wing shape and surface finish. By introducing the surface roughness, the laminar boundary layers can be perturbed or become turbulent and are thus more resistible to the adverse pressure gradient. In such a way, the separation can be delayed or avoided.

Surface roughness has been adopted as a method of altering the flow pattern in various types of flows. Saric et al. [3,4] used surface roughness as a means of passive flow control in experimental studies of transition flow over swept wings. White and Saric [5] examined roughness effects on transition and found that three-dimensional static roughness can be an effective tool in delaying the transition to turbulence on a swept wing by distributing roughness elements at a spacing approximately equal to one-half of the spanwise wavelength of the critical mode. Carpenter et al. [6,7] continued the work of Saric et al. [3] and found that the flow is very sensitive to both the shape and height of the discrete roughness elements. In the experimental study of unsteady and transitional flows behind roughness elements in Ergin and White [8], it is found that with the increase of roughness height, the initial amplitudes of the steady disturbances and the growth rates of the unsteady disturbances increase. It should be noted that the Reynolds numbers for experimental investigations were usually much higher than that of the present study. The surface roughness was also applied in altering the supersonic flows (e.g., [9,10]). At Mach 2.8, Latin and Bowersox [10] found that as the roughness height was increased, the turbulence production relative to the frictional losses increased. Fransson et al. [11,12] applied roughness elements on a flat plate in a wind tunnel and found that this passive control technique can delay transition to turbulence. Zhang et al. [13] experimentally investigated the performance degradation of a low-Reynolds-number airfoil with distributed leading-edge roughness and found that the roughness height appears to be a more critical factor for roughness induced performance degradation than other factors such as distribution patterns. Honsaker and Huebsch [14] used a Prandtl transposition to model the surface roughness on airfoils and found that the dynamic surface roughness is effective on the stall separation control. Rizzetta and Visbal [15] employed a high-order overset-grid approach to model cylindrical roughness elements and studied the flow past an array of distributed roughness elements. More recently, Rizzetta et al. [16] performed a direct numerical simulation of discrete roughness on a swept-wing leading edge and studied the stability of crossflow with roughness. Redford et al. [17] studied the compressibility effects on boundary-layer transition induced by an isolated roughness element and suggested that the boundary layer near the roughness element is particularly receptive to external disturbances.

Surface roughness is also applied in controlling flow separation. Santhanakrishnan and Jacob [18] investigated the separation behavior with large-scale roughnesses on an airfoil surface and showed that the separation is delayed and the separation region is smaller for the perturbed airfoil case at moderate Reynolds number and higher angle of attack. Boiko et al. [19] experimentally applied surface humps for the control of laminar separated flows and suggested that the injection of stationary disturbances in the separation region followed by their transient amplification is a promising way of flow control. It was found that with a suitable size of the roughness elements placed close to separation line and spanwise spacing between them, it is possible to generate streamwise stationary disturbances subject to transient growth accompanied by secondary instability to unsteady disturbances promoting laminar flow breakdown.

High-order methods on unstructured grids are known for their advantages of accuracy and flexibility in the numerical simulation of multiscale flow with complex geometries. In the last two decades, there have been intensive research efforts on high-order methods for unstructured grids [20–32]. In this paper, a high-order spectral difference (SD) method for the three-dimensional Navier–Stokes equations on unstructured hexahedral grids developed by Sun et al. [32] is used. This approach is capable of capturing the laminar separation and the vortex breakdown and has been previously shown in the numerical simulation of the attached/detached laminar flow and the reattached turbulent flow in the case of the uncontrolled baseline model (also see [33]).

In this paper, a passive flow control technique using surface roughness (bumps) near the leading edge of the wing is numerically studied. The roughness bumps can affect the formation of the LSBs and be used for the purpose of aerodynamic performance improvement. The flow over a SD7003 wing at AOA $= 4$ deg, $Re_c = 6 \times 10^4$ and $M = 0.2$ is used as the baseline model and the starting point for the controlled models. The rest of the paper is organized as follows. In the next section, the spectral difference method on unstructured hexahedral mesh is briefly reviewed. In Sec. III, numerical results of the baseline model are presented and the flow features associated with LSBs are discussed. In Sec. IV, a series of cases with different bump sizes, bump numbers, and angles of attack are numerical simulated. The numerical results of the controlled cases are compared with those of the baseline model and the detail effects of the surface roughness are investigated. Concluding remarks are given in Sec. V.

II. Review of Multidomain Spectral Difference Method

A. Governing Equations

Consider the three-dimensional compressible nonlinear Navier–Stokes equations written in the conservation form as

$$\frac{\partial Q}{\partial t} + \frac{\partial F}{\partial x} + \frac{\partial G}{\partial y} + \frac{\partial H}{\partial z} = 0 \tag{1a}$$

on domain $\Omega \times [0, T_0]$ and $\Omega \subset R^3$ with the initial condition

$$Q(x, y, z, 0) = Q_0(x, y, z) \tag{1b}$$

and appropriate boundary conditions on $\partial\Omega$.

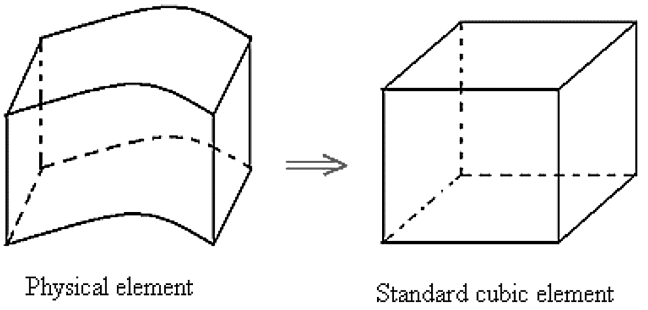

Fig. 1 Transformation from a physical element to a standard element.

B. Coordinate Transformation

In the SD method, it is assumed that the computational domain is divided into nonoverlapping unstructured hexahedral cells or elements. To handle curved boundaries, both linear and quadratic isoparametric elements are employed, with linear elements used in the interior domain and quadratic elements used near high-order curved boundaries. To achieve an efficient implementation, all physical elements (x, y, z) are transformed into standard cubic element $(\xi, \eta, \varsigma) \in [-1, 1] \times [-1, 1] \times [-1, 1]$, as shown in Fig. 1.

The transformation can be written as

$$\begin{bmatrix} x \\ y \\ z \end{bmatrix} = \sum_{i=1}^{K} M_i(\xi, \eta, \varsigma) \begin{bmatrix} x_i \\ y_i \\ z_i \end{bmatrix} \tag{2}$$

For the transformation given in Eq. (2), the Jacobian matrix J takes the following form:

$$J = \frac{\partial(x, y, z)}{\partial(\xi, \eta, \varsigma)} = \begin{bmatrix} x_\xi & x_\eta & x_\varsigma \\ y_\xi & y_\eta & y_\varsigma \\ z_\xi & z_\eta & z_\varsigma \end{bmatrix}$$

The governing equations in the physical domain are then transformed into the standard element, and the transformed equations take the following form:

$$\frac{\partial \tilde{Q}}{\partial t} + \frac{\partial \tilde{F}}{\partial \xi} + \frac{\partial \tilde{G}}{\partial \eta} + \frac{\partial \tilde{H}}{\partial \varsigma} = 0 \tag{3}$$

where

$$\tilde{Q} = |J| \cdot Q \qquad \begin{bmatrix} \tilde{F} \\ \tilde{G} \\ \tilde{H} \end{bmatrix} = |J| \begin{bmatrix} \xi_x & \xi_y & \xi_z \\ \eta_x & \eta_y & \eta_z \\ \varsigma_x & \varsigma_y & \varsigma_z \end{bmatrix} \cdot \begin{bmatrix} F \\ G \\ H \end{bmatrix}$$

C. Spatial Discretization

In the standard element, two sets of points are defined (namely, the solution points and the flux points), illustrated in Fig. 2 for a 2-D element. The solution unknowns Q or degrees of freedom (DOF) are stored at the solution points, while fluxes are computed at the flux points. The solution points in 1-D are chosen to be the Gauss points defined by

$$X_s = \cos\left(\frac{2s-1}{2N}\pi\right), \qquad s = 1, 2, \ldots, N \tag{4}$$

With solutions at N points, we can construct a degree $(N-1)$ polynomial in each coordinate direction using the following Lagrange basis defined as

$$h_i(X) \prod_{s=1, s\neq i}^{N} \left(\frac{X - X_s}{X_i - X_s}\right) \tag{5}$$

The reconstructed solution for the conserved variables in the standard element is just the tensor products of the three one-dimensional polynomials, i.e.,

$$Q(\xi, \eta, \varsigma) = \sum_{k=1}^{N}\sum_{j=1}^{N}\sum_{i=1}^{N} \frac{\tilde{Q}_{i,j,k}}{|J_{i,j,k}|} h_i(\xi) \cdot h_j(\eta) \cdot h_k(\varsigma) \tag{6}$$

The flux points in 1-D are chosen to be the $(N-1)$ Gauss quadrature points plus the two ending points. With fluxes at $(N+1)$ points, a degree N polynomial can be constructed in each coordinate direction using the following Lagrange bases defined as

$$l_{i+1/2}(X) \prod_{s=0, s\neq i}^{N} \left(\frac{X - X_{s+1/2}}{X_{i+1/2} - X_{s+1/2}}\right) \tag{7}$$

Similarly, the reconstructed flux polynomials take the following form:

$$\tilde{F}(\xi, \eta, \varsigma) = \sum_{k=1}^{N}\sum_{j=1}^{N}\sum_{i=0}^{N} \tilde{F}_{i+1/2,j,k} l_{i+1/2}(\xi) \cdot h_j(\eta) \cdot h_k(\varsigma) \tag{8a}$$

$$\tilde{G}(\xi, \eta, \varsigma) = \sum_{k=1}^{N}\sum_{j=0}^{N}\sum_{i=1}^{N} \tilde{G}_{i,j+1/2,k} h_i(\xi) \cdot l_{j+1/2}(\eta) \cdot h_k(\varsigma) \tag{8b}$$

$$\tilde{H}(\xi, \eta, \varsigma) = \sum_{k=0}^{N}\sum_{j=1}^{N}\sum_{i=1}^{N} \tilde{H}_{i,j,k+1/2} h_i(\xi) \cdot h_j(\eta) \cdot l_{k+1/2}(\varsigma) \tag{8c}$$

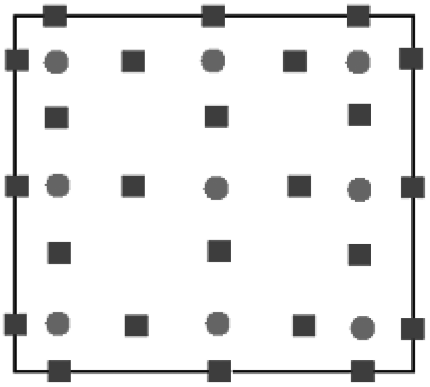

Fig. 2 Distribution of solution points (circles) and flux points (squares) in a standard element for a third-order SD scheme.

D. Algorithm

Because the SD method is based on the differential form of the governing equations, the implementation is straightforward even for high-order curved boundaries. All the operations are basically one-dimensional in each coordinate direction and each coordinate direction shares the collocated solution points with others, resulting in improved efficiency. In summary, the algorithm to compute the inviscid flux and viscous flux and update the unknowns (DOF) consists of the following steps:

1) Given the conserved variables $\{Q_{i,j,k}\}$ at the solution points, compute the conserved variables $\{Q_{i+1/2,j,k}\}$ at the flux points using polynomial (6). Note that inviscid flux is a function of the conserved solution and the viscous flux is a function of both the conserved solution and its gradient, taking flux $\tilde{F}$; for example,

$$\begin{cases} \tilde{F} = \tilde{F}^i - \tilde{F}^v \\ \tilde{F}_{i+1/2,j,k} = \tilde{F}^i(Q_{i+1/2,j,k}) \\ \tilde{F}^v_{i+1/2,j,k} = \tilde{F}^v(Q_{i+1/2,j,k}, \nabla Q_{i+1/2,j,k}) \end{cases} \tag{9}$$

2) Compute the inviscid fluxes $\{\tilde{F}^i_{i+1/2,j,k}\}$ at the interior flux points using the solution $\{Q_{i+1/2,j,k}\}$ computed at step 1. Compute

the viscous fluxes $\{\tilde{F}^v_{i+1/2,j,k}\}$ using the solution $\{Q_{i+1/2,j,k}\}$ computed at step 1 and the gradient of the solutions $\{\nabla Q_{i+1/2,j,k}\}$ computed based on $\{Q_{i+1/2,j,k}\}$.

3) Compute the common inviscid flux at element interfaces using a Riemann solver (10), such as the Roe solver [34] and Russanov solver [32]:

$$\tilde{F}^i = \tilde{F}^i(Q_L, Q_R) \tag{10}$$

Compute the common viscous flux at element interfaces using a viscous approach [Eq. (11)], such as the averaged approach and discontinuous-Galerkin-like approach [32]:

$$\tilde{F}^v = \tilde{F}^v(Q_L, Q_R, \nabla Q_L, \nabla Q_R) \tag{11}$$

Then compute the derivatives of the fluxes at all the solution points by using Eq. (12):

$$\left(\frac{\partial \tilde{F}}{\partial \xi}\right)_{i,j,k} = \sum_{k=1}^{N}\sum_{j=1}^{N}\sum_{i=0}^{N} \tilde{F}_{i+1/2,j,k} l'_{r+1/2}(\xi_i)\cdot h_j(\eta)\cdot h_k(\varsigma) \tag{12a}$$

$$\left(\frac{\partial \tilde{G}}{\partial \eta}\right)_{i,j,k} = \sum_{k=1}^{N}\sum_{j=0}^{N}\sum_{i=1}^{N} \tilde{G}_{i,j+1/2,k} h_i(\xi)\cdot l'_{r+1/2}(n_j)\cdot h_k(\varsigma) \tag{12b}$$

$$\left(\frac{\partial \tilde{H}}{\partial \varsigma}\right)_{i,j,k} = \sum_{k=0}^{N}\sum_{j=1}^{N}\sum_{i=1}^{N} \tilde{H}_{i,j,k+1/2} h_i(\xi)\cdot h_j(\eta)\cdot l'_{r+1/2}(\varsigma_k) \tag{12c}$$

4) Update the DOF using a multistage total-variation-diminishing scheme for time integration of Eq. (13):

$$\frac{\partial \tilde{Q}_{i,j,k}}{\partial t} = -\left(\frac{\partial \tilde{F}}{\partial \xi} + \frac{\partial \tilde{G}}{\partial \eta} + \frac{\partial \tilde{H}}{\partial \varsigma}\right)_{i,j,k} \tag{13}$$

For more details about SD method on hexahedral mesh, the readers can refer to [30].

III. Baseline Model

The flow over the SD7003 wing at AoA = 4 deg, Reynolds number $Re_c = 6 \times 10^4$ and Mach number $M = 0.2$ without surface roughness is used as the baseline model. This case is chosen due to the variety of previously experimental and numerical results [35,36]. The baseline model is numerically simulated first and then the results are used to compare with and assess the performance of the controlled models in the next section. The computational grid and boundary conditions are introduced below, and a p-type grid resolution study is carried out. The statistical numerical results are presented. Then the features associated with the LSBs and the mechanisms of turbulent transition are discussed.

In this paper, the Reynolds number and Mach number are fixed for all the cases. The cases with different geometries and parameters are named according to the AOA, with or without bumps and the additional bump parameters; e.g., AOA_4c represents the controlled case at AOA = 4 deg, and AOA_4 refers to the current case of the baseline model.

A. Computational Grid and Boundary Conditions

Figure 3 shows the computational grid for the baseline case AOA_4. To model a wing with an infinite-span, a periodic boundary condition is used in the spanwise direction and the span width of the wing is chosen to be 20% of the chord, which was shown to be wide enough in [33,35]. A no-slip adiabatic boundary condition is applied on the surface of the wing. The outflow boundary is set to be five chord lengths away from the airfoil, and at the far field of the computational domain, an absorbing sponge zone (ASZ) boundary condition [37] is imposed. The total number of cells used in the present study is 253,600 for the baseline model, resulting in 6,847,200 and 16,230,400 DOF per equation for the third-order and fourth-order SD schemes, respectively. Fine-grid cells are generated near the wall and around the physically important region where the separation bubble and vortex breakdown occur. The smallest cells are located on the surface of the airfoil and the mesh size grows gradually in the normal direction. Based on the mean skin-friction value at the turbulent flow region ($x = 0.750.95$), the dimensions of the smallest cell in wall units are $\Delta y^+_{\text{cell}} = 3.0$–$4.0$ in the normal direction, $\Delta x^+_{\text{cell}} = 30.0$–$40.0$ in the flow direction and $\Delta z^+_{\text{cell}} = 15.0$–$20.0$ in the spanwise direction. Inside each cell the mesh is further discretized by 4 f.u. points in the third-order SD scheme and by 5 f.u. points in the fourth-order SD scheme. The extra DOF within each cell effectively decrease the y^+ number by a factor of 5 for the third-order scheme and a factor of 9 for the fourth-order scheme. Therefore, the resolution of the current mesh is close to what is required of a direct numerical simulation.

Parallel computation with message passing interface (MPI) is employed in the simulations of the present paper, and the mesh is partitioned into zones with a nearly equal number of cells using a coordinate bisection algorithm. Because of the compactness of the SD method, the communication between two cells occurs only on their shared interface through the collocated flux points. The decomposition of unstructured meshes is easier and more straightforward comparing with the decomposition of structured meshes. The scalability of the current code is excellent with a parallel efficiency over 98% for problems simulated in this paper. Typically, the wall-clock time on a mesh of 125,000 cells is about one week for

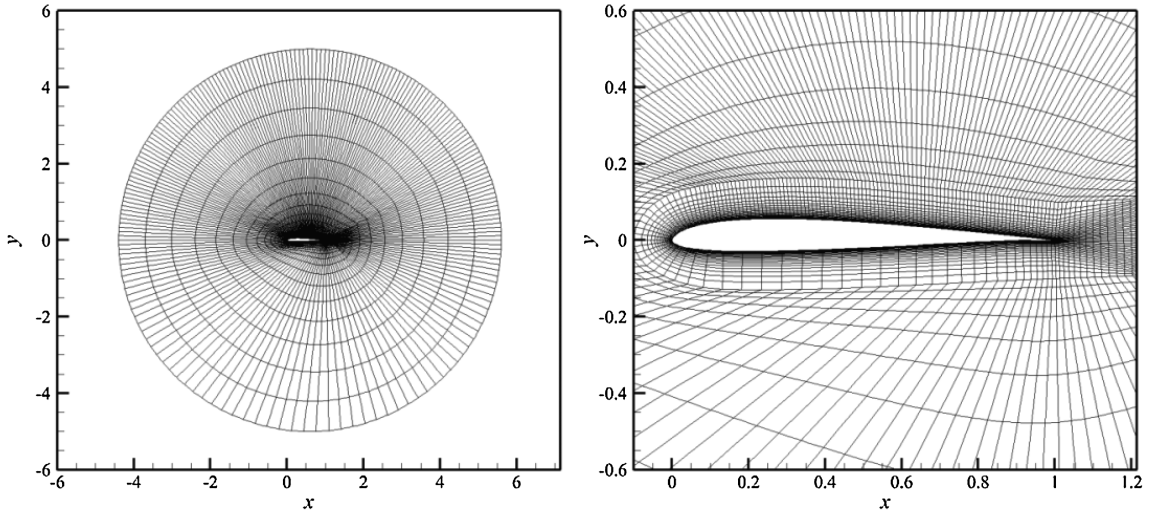

Fig. 3 Computational mesh.

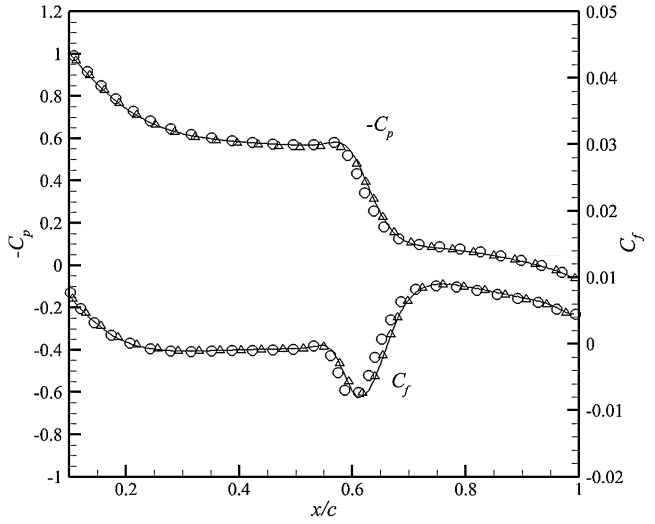

Fig. 4 Mean pressure coefficient) and mean skin-friction coefficient on the wing surface; fourth-order result on grid 1 (solid line), third-order result on grid 1 (circles), and third-order result on grid 2 (delta symbols).

the third-order scheme and 2–3 weeks for the fourth-order scheme on 32 INTEL Xeon E5530 CPUs.

B. Averaged and Statistical Results

To further verify the resolution of the computational mesh (Fig. 3), a grid refinement study is carried out. An increasing of the polynomial order in each element from 2 (resulting in third-order accuracy) to 3 (resulting in fourth-order accuracy), the so-called polynomial order (p-type) refinement study, is first performed for the baseline case AOA_4. An additional numerical simulation using the third-order SD scheme is carried out on a verification mesh with a total of n DOF of 15,836,600 per equation, which is very close to the n DOF for the fourth-order SD scheme on the previous mesh, and the hexahedral cell size has been scaled down accordingly. At the meantime, the outflow boundary of grid 2 is set to be 20 chord lengths away from the airfoil with a fixed freestream boundary condition to verify the effectiveness of the far-field ASZ boundary condition. This could be regarded as an h-type refinement grid study, and here we call the mesh shown in Fig. 3 grid 1 and the verification mesh grid 2.

In Fig. 4, the mean pressure coefficient C_p and the mean skin-friction coefficient C_f distributions on the wing surface for the grid refinement study are shown. In the present numerical simulations, the mean flowfield and the statistical results are obtained by averaging the instantaneous flowfield over eight nondimensional time units. A very good agreement between the fourth-order results on grid 1 and the third-order results on grid 2 has been found in Fig. 4, and the agreement in the p-type refinement study on grid 1 is also good, except in the separated breakdown region. Table 1 compares the locations of separation, transition, and reattachment in the grid refinement study cases. The onset location of transition is defined by a critical value of 0.001 of the normalized Reynolds stress τ_{xy} as used in [35,36,38–40]. The differences between the above measurements are all less than 2%. The results from Galbraith and Visbal [35] under the same flow condition are listed here and the agreement is also good. Several particle image velocimetry (PIV) experiments were carried out in [36] on SD7003 airfoil with the same Reynolds number and AOA. The results from the available experimental PIV data [36] are also included in Table 1 for comparison. The differences are expected to be due to the existence of freestream turbulence and surface roughness in the experiments.

Table 1 Separation, transition, and reattachment locations

Case	Separation	Transition	Reattachment
Third-order on grid 1	0.223	0.515	0.675
Fourth-order on grid 1	0.227	0.521	0.685
Third-order on grid 2	0.225	0.525	0.683
Galbraith and Visbal [35]	0.23	0.55	0.65
IAR [36]	0.33	0.57	0.63
TU-BS [36]	0.30	0.53	0.62
AFRL [36]	0.18	0.47	0.58

C. Flow Features Associated with the Laminar Separation and Turbulent Transition

Figure 5a displays the mean streamlines around the wing and the mean streamwise velocity field averaged in both time and the spanwise direction. The mean separation bubble and the reattachment of the flow are clearly shown. In Fig. 5b, the negative value of the mean spanwise vorticity on the suction surface of the wing at interval $x = [0.0, 0.6]$ represents the laminar shear layer before the flow transitions into turbulent flow. The amplitude of the disturbance inside this interval has been found to grow exponentially due to the Kelvin–Helmholtz instability after separation [33,36,39,40]. The shear layer terminates around $x = 0.65$ at the end of the time-mean LSB (Fig. 5a), where the vortex breakdown occurs. A turbulent boundary layer forms at interval $x = [0.75, 1.0]$. Figures 5c and 5d show the statistical distribution of the normalized turbulent kinetic energy (TKE) and the normalized Reynolds stress τ_{xy}, respectively. Results of both third-order and fourth-order SD schemes are shown and are reasonably close to each other. The mean streamwise velocity field and the normalized Reynolds stress (τ_{xy}) distribution from available experimental PIV data from the U.S. Air Force Research Laboratory (AFRL) [36] are presented in Fig. 5e for comparison. The computed results agree well with the measured results [also see the data from the Institute for Aerospace Research (IAR) and Technische Universität Braunschweig (TU-BS) in [36]] in terms of shape, magnitude, and extent. The concentration of both TKE and τ_{xy} around $x \approx 0.65$ is strongly related to the process of vortex breakdown and is discussed later in this section.

Figure 6 shows the profiles of the mean tangential velocity u_t at different locations and the corresponding profiles of rms tangential velocity disturbance u_t' at the corresponding locations of the baseline model. The development of the mean shear layer from an attached layer to a detached one can be clearly seen. The profiles of rms of u_t' vary along with the mean shear layer. After separation, the inflection point gradually shows in the mean velocity profiles (Fig. 6a) and the K-H instability becomes dominant accompanied by the vortex shedding.

Figure 7 shows the instantaneous contour lines of the Q-invariant [41] for about a shedding period. Inside the detached shear layer (Fig. 5b), vortical tubes (rolls) are shed and grow convectively, as shown in Fig. 7. The K-H instability is also called inviscid instability, in which the disturbance is more unstable in two dimensions than in three dimensions. The shedding vortices remain two-dimensional until entering the breakdown stage.

It is observed that two-dimensional vortices break down to small-scale structures rapidly in the region $x = [0.6, 0.7]$, as shown in Fig. 7. And in the same region, the skin friction and the wall pressure increase suddenly (Fig. 4). Finally the flow reattaches to the wall and the laminar separation is terminated by turbulent flow. As shown in Fig. 7, the vortex breakdown process extends from the bottom to the top and the small-scale structures close to the wall at interval $x = [0.6, 0.7]$ with upstream-going velocity play an important role in this process. A layer of small-scale structures stay near the wall in this region right below the shedding vortices. As the layer remains within the separation bubble region, the small-scale structures move upstream due to the reversed flow direction. When the shedding vortices pass the region, the bottom part of the shedding vortices meets and interacts with the upstream-going small-scale structures. The bottom part of the vortices breaks down to small-scale structures first, then the upper part is affected and breaks down by the swirling motion of the vortices. In such a way, the vortex tube breaks down from the bottom to the top due to a feedback mechanism [33]. After the breakdown of the large-scale vortices into smaller-scale eddies, the flow becomes turbulent. Spalart and Strelets [42] concluded this process as a simple mechanism of transition by contact. Jones et al.

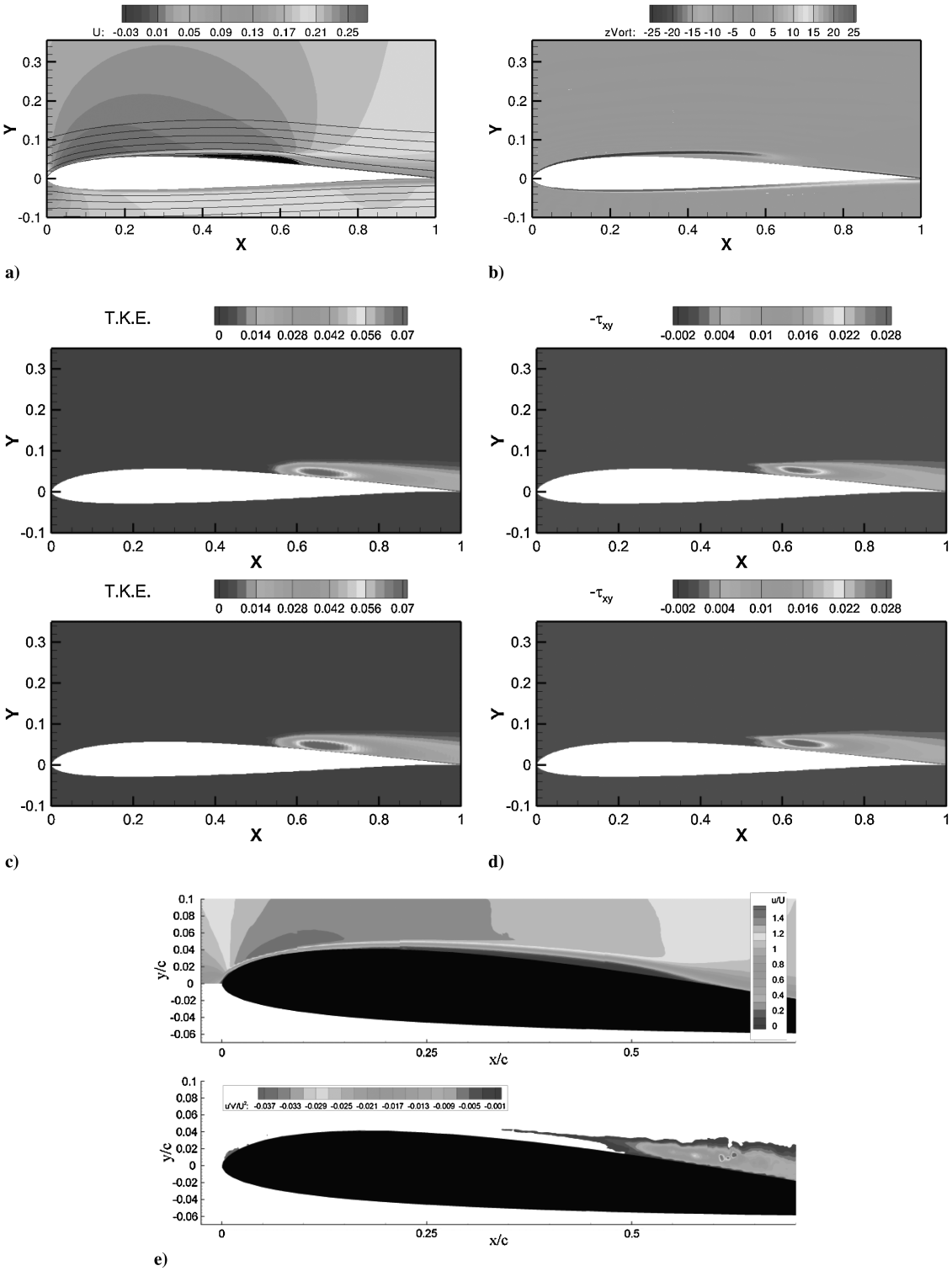

Fig. 5 Mean and statistical results of baseline model: a) mean streamlines around the wing and mean streamwise velocity field, b) mean spanwise vorticity field, c) normalized TKE distribution (upper: third-order SD scheme; lower: fourth-order scheme), d) normalized Reynolds stress (τ_{xy}) distribution (upper: third-order SD scheme; lower: fourth-order scheme), e) mean streamwise velocity field and the normalized Reynolds stress (τ_{xy}) distribution from available experimental PIV data from the AFRL [36].

[43] attributed a similar process to be caused by the three-dimensional absolute instability.

The contours of the normalized mean total pressure P_{Total}, the mean pressure coefficient C_p distribution and the pressure gradient magnitude $|\nabla P|$ for the case AOA_4 are shown in Fig. 8. Both the total pressure and the static pressure are almost constant inside the separation region and are lower inside the LSB than those outside the LSB. In other words, in the averaged sense the LSB persists a constant low pressure inside and is pressed by high pressure outside. Around the location $x = 0.65$, there exists a region of high adverse pressure gradient (APG), as shown in Fig. 8c, and a high-pressure gradient terminates the LSB. This region around $x = 0.65$ is exactly the same region where the breakdown and reattachment are observed. In the sense of the mean flowfield, the pressure difference is balanced by the friction force over the wall, as shown in Fig. 4. The TKE and τ_{xy} are also found to be concentrated in the same region, as shown in Figs. 5c and 5d. The above features illustrate that this region is physically important to the formation of the LSB and the

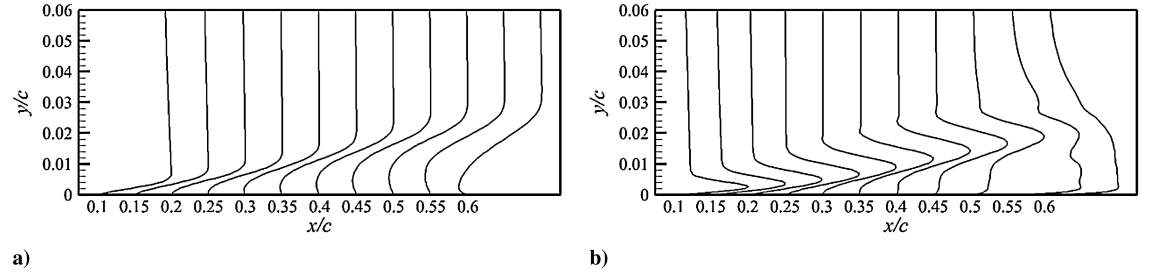

Fig. 6 Numerical results for baseline model: a) normalized profiles of the mean tangential velocity at different locations, b) normalized profiles of rms tangential velocity disturbances at different locations. The x-axis indicates the location of the profile and each profile is displaced by 0.05.

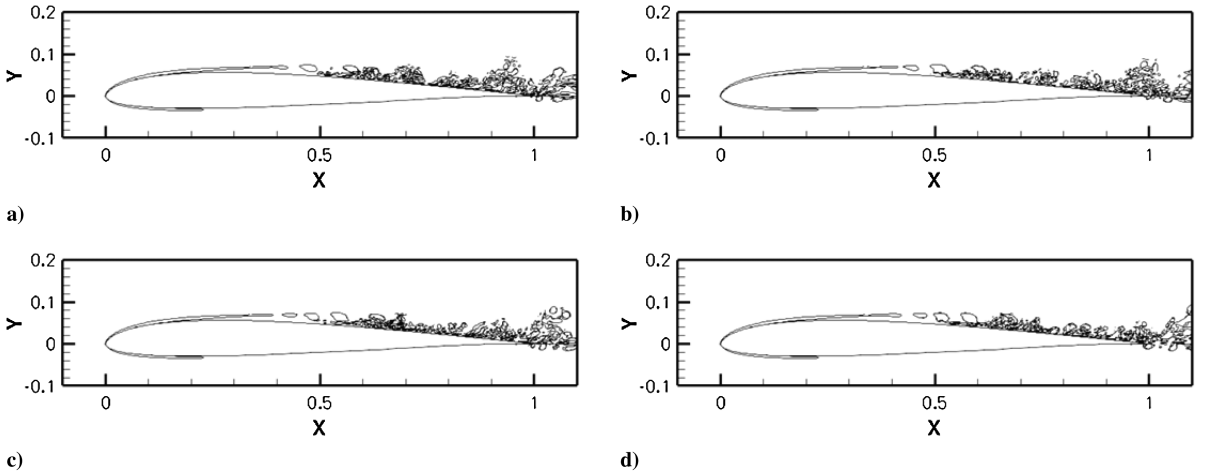

Fig. 7 Instantaneous contour line of $Q = 1$ for about one shedding period.

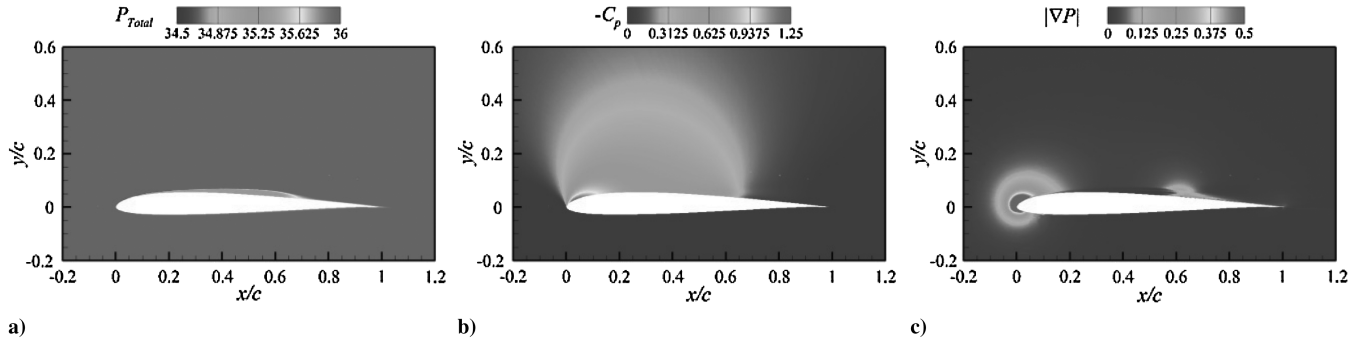

Fig. 8 Averaged numerical results of case AOA_4: Contours of a) normalized total pressure P_{Total}, b) pressure coefficient $-C_p$, and c) pressure gradient magnitude $|\nabla P|$.

breakdown process thereafter, to which the attention should be paid when investigating the effects of the surface roughness. It will be shown later that the typical feature of the sudden recovery of pressure and the associated separation in region $x = [0.6, 0.7]$ on the suction side of the baseline model can be altered with the surface roughness.

IV. Effects of Surface Roughness

The numerical simulations of the surface roughness effects are carried out in this section. The study can help improve the design of future passive control devices on the wing surface for separation control and drag reduction.

By using the high-order SD method on unstructured hexahedral mesh, geometry of the roughness bumps are modeled, as shown in Fig. 9a. The bump geometry is defined using the following parameters: the width W_{AC}, the length L_{BD} and the height H_{EF} of the bump. The surface edges of the bump are tangentially patched with the wing surface by high-order (P_3) polynomial curves and the curved surface on the top (at point F) of the bump is also tangential to the original wing surface at point E, as shown in Fig. 9b. Above the surface of the bump the smallest grid size remains the same as in the baseline case, and near the leading edge the mesh distribution around the bump is shown in Fig. 9c. In all cases, the discrete roughness bumps are equally spaced near the leading edge before the flow separates. Cases with different geometries, numbers of roughness bumps, and AOA are considered and numerically investigated.

A. Effects of Roughness Bump Size

Three cases with different roughness geometries are simulated and presented to test the effects of the bump size. The geometric parameters of the roughness bumps in all three cases are shown in Table 2. To affect the attached boundary-layer profile before separation and also not induce too much viscous drag force, the location and dimension of the bumps in case AOA_4c are chosen after several tests. Through trial and error, the bump size and height were found to affect the flow more than the bump location. Here in all cases, the bumps are placed at a fixed location $x = 0.05$, where the boundary-layer thickness for the baseline model AOA_4 is $\delta_E = 0.0049$. The

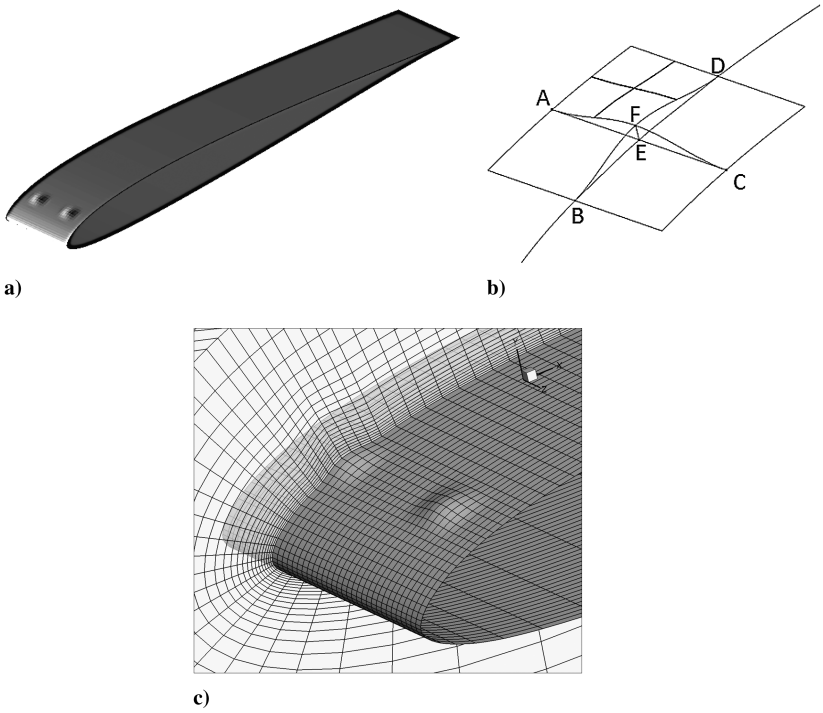

Fig. 9 a) Roughness bump on the wing surface, b) bump geometries, and c) mesh distribution around the bump.

cases AOA_4c.w and AOA_4c.h are variations based on case AOA_4c. The bumps in AOA_4c.w are twice as wide (W_{AC}) as in AOA_4c. In cases AOA_4c and AOA_4c.w, the height of the bumps is about 70% of the boundary-layer thickness δ_E, while in case AOA_4c.h the height is set to close to 100% δ_E.

The instantaneous isosurfaces and side views of the Q-invariant are shown in Fig. 10 for the baseline model and the cases with roughness bumps. The effectiveness of the bumps in changing the flowfield of the baseline model can be clearly seen. In case AOA_4c, vortex shedding in the separation bubble region is observed as in the baseline model AOA_4. However, the shedding vortices are distorted, as streamwise vorticities are generated behind the bumps. The shedding vortices are closer to the airfoil surface and the frequency of vortex shedding is higher than those in the baseline model, as shown in Fig. 10b. It is found in both AOA_4c.w and AOA_4c.h that small-scale vortex packets are generated behind the bumps and the pattern is periodic (Figs. 10c and 10d). This implies that changing the width and height of the bumps can dramatically change the flow features, and the wider and taller bumps introduce stronger disturbances and significantly affect the laminar boundary-layer flow. The perturbed region (periodic vortical packets) after the bumps grows in the flow direction, takes over the laminar region. Eventually the boundary layer becomes fully turbulent, as shown in Figs. 10c and 10d. Vortex shedding is also found in the laminar region of the flow, and the shedding vortical rolls interact with the adjacent turbulent region. In cases AOA_4c.w and AOA_4c.h, the roughness bump act like the turbulators, and the breakdown process is triggered by the vertical packets generated right behind the bumps, as shown in Figs. 10c and 10d.

The mean pressure coefficient and friction coefficient distributions on the suction surface of the controlled cases are shown in Fig. 11,

Table 2 Parameters of the roughness bumps for effects of roughness bump size

Case	X_E	W_{AC}	L_{BD}	H_{EF}	N_{bump}	δ_E
AOA_4	N/A	N/A	N/A	N/A	N/A	0.0049
AOA_4c	0.05	0.045	0.045	0.0035	2	N/A
AOA_4c.w	0.05	0.090	0.045	0.0035	2	N/A
AOA_4c.h	0.05	0.045	0.045	0.005	2	N/A

compared with the results of the baseline model. As shown in the friction coefficient plots, the separation region is smaller in case AOA_4c than in the baseline model. Disturbed by the upstream bumps, flow separation is delayed, while the breakdown and reattachment occur at an earlier location. In case AOA_4c, the features associated with the LSB, which include a pressure plateau and steep pressure recovery at the strong separation region, are also observed in $x = [0.5, 0.6]$. This indicates the characteristics of the breakdown process in AOA_4c are quite similar to those in the baseline model AOA_4 even though the flowfield is disturbed by the streamwise vorticity generated by the bumps. And the feedback mechanism of the circulation flow serves the same important role in the breakdown process of case AOA_4c as in the baseline model. With the increase of the width or height of roughness bumps, the LSBs are completely avoided in cases AOA_4c.w and AOA_4c.h, as shown in the friction coefficient plot of Fig. 11. A similar trend can be found in the cases of separation active control by increasing the magnitude of suction/blowing [44] and also in the cases by increasing the freestream turbulence level [45]. In cases AOA_4c.w and AOA_4c.h, the pressure recovers smoothly (Fig. 11) without separation and the breakdown process occurs convectively (Figs. 10c and 10d). The pressure recovery and the associated strong separation region ($x = [0.6, 0.7]$ for case AOA_4 and $x = [0.5, 0.6]$ for case AOA_4c) seem to be closely related to the LSBs. Figure 12 shows the contours of the pressure gradient magnitude for cases AOA_4c and AOA_4c.h. With a reduced separation region in case AOA_4c, the severe APG region (Fig. 12a) can also be observed in $x = [0.5, 0.6]$ but is weaker than that in case AOA_4. In case AOA_4c.h, the severe APG region $x = [0.5, 0.6]$ disappears when the separation is avoided (Fig. 12b). And in case AOA4.w the situation is similar to case AOA_4.h.

Table 3 presents the mean lift and drag coefficients per unit span and the lift-to-drag ratio of all the cases. The drag coefficients decrease for all the controlled cases, and the lift coefficients also decrease slightly. It can be seen in Figs. 10 and 11 that roughness bumps generate a larger turbulent flow region, and thus the friction drag increases. The contribution to the drag C_D from both pressure drag C_{Dp} and friction drag C_{Df} are also listed in Table 3 for all the cases. It is shown that with the reduction of the separation region, the pressure drag C_{Dp} decreases and the friction drag C_{Df} increases. However, the pressure drag decreases by a larger amount than the

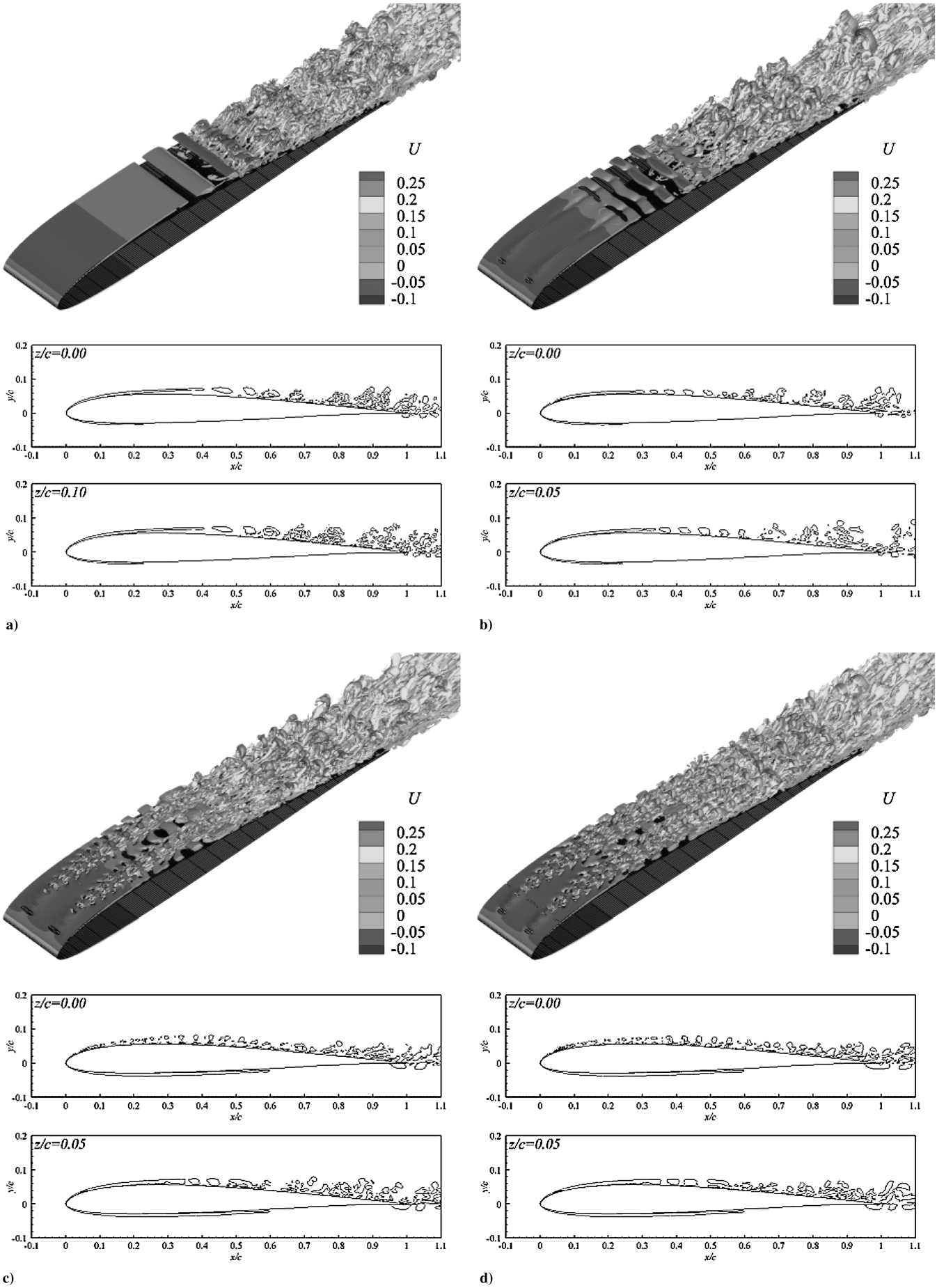

Fig. 10 Isosurface of Q-invariant colored by streamwise velocity and side view: a) AOA_4, b) AOA_4c, c) AOA_4c.w, d) AOA_4c.h.

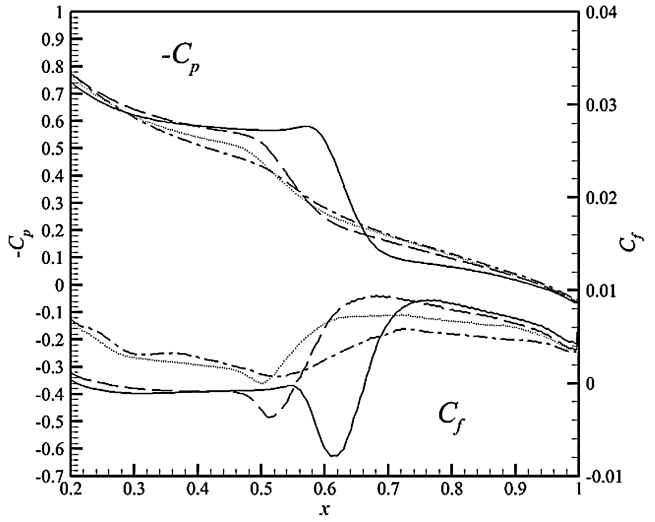

Fig. 11 Mean pressure coefficient and mean skin-friction coefficient on the wing surface; AOA_4 (solid line), AOA_4c (dashed line), AOA_4c.w (dash-dotted line) and AOA_4c.h (dotted line).

Table 3 Mean lift coefficient, drag coefficient (per unit span), and lift-to-drag ratio

Case	C_L	C_D	C_{Dp}	C_{Df}	L/D
AOA_4	0.600	2.34e − 2	1.38e − 2	0.97e − 2	25.6
AOA_4c	0.593	2.05e − 2	1.00e − 2	1.05e − 2	28.9
AOA_4c.w	0.579	2.10e − 2	0.94e − 2	1.16e − 2	27.6
AOA_4c.h	0.579	2.07e − 2	0.95e − 2	1.12e − 2	28.0

Table 4 Parameters of the roughness bumps for effects of the number of bumps

Case	X_E	W_{AC}	L_{BD}	H_{EF}	N_{bump}	δ_E
AOA_4	N/A	N/A	N/A	N/A	N/A	0.0049
AOA_4c.1	0.05	0.045	0.045	0.0035	1	N/A
AOA_4c	0.05	0.045	0.045	0.0035	2	N/A
AOA_4c.4	0.05	0.045	0.045	0.0035	4	N/A
AOA_4c.4n	0.05	0.0225	0.045	0.0035	4	N/A

increase of friction drag resulting in an overall drag reduction of over 10%. In addition, the lift-to-drag ratio is increased by at least 10% for all the controlled cases, as shown in Table 3.

As listed in Table 3, case AOA_4c appears to produce the base value of the L/D ratio, even though in this situation the separation is still laminar. Although both the lift force and the pressure induced drag force decrease with the diminishing of the separation zone, the turbulent flow region triggered by the bumps in cases AOA_4c.w and AOA_4c.h has brought a larger increase in the friction drag force. In comparison with case AOA_4c, the resulting overall drag force in cases AOA_4c.w and AOA_4c.h is higher and the lift force is also a bit lower. Thus, the L/D ratio of the case AOA_4c is larger than these in cases AOA_4c.w and AOA_4c.h.

B. Effects of the Number of Bumps

Geometric parameters of the roughness bumps in the cases of this section are shown in Table 4. Case AOA_4c has two roughness bumps on the span width of 20% chord length and it is again used as the starting point for variations. Cases AOA_4c.1 and AOA_4c.4 have just one and four bumps on the same span width with everything else remaining the same. Case AOA_4c.4n reduces the bump width W_{AC} by 50% and double the number of bumps from two to four, which is for further comparison with the cases AOA_4c and AOA_4c.4. Figure 13 shows the instantaneous isosurface and side view of Q-invariant of all the cases. Similar to case AOA_4c (Fig. 13b), the attached boundary layer and the following shedding vortices are perturbed but still remain laminar for all the cases. Vortex shedding due to the K-H instability occurs in all the cases and the turbulent vortical packet formed in cases AOA_4c.w and AOA_4c.h is not observed here. The number of bumps N_{bump} affects the spanwise wavelength of the disturbance. After separation, the K-H instability takes the dominant role of disturbance growth and the most unstable mode of K-H instability, which is also called inviscid instability is two-dimensional and the spatial growth rate of the disturbance decreases with the increase of the spanwise wave number [44]. Thus, the physics and mechanisms are associated with the three-dimensional instability in the detached shear layer and also possibly the elliptical instability [43,46] of the shedding vortices.

Figure 14 shows the instantaneous contours of u velocity and streamwise vorticity on the cutting plane at $y = 0.065$ for all the cases. It can be seen that high-speed flow is induced away behind the bumps. And low-speed regions between bumps are actually part of the separation interval in the baseline case. It is known that wakes are generated behind bluff bodies and airfoils and the flow speed decreases. The flow behind bumps is similar. In a close region behind the bump, it is observed that a wake is induced and flow speed decreases. However, the flow in the separated region is found to be speeding up instead of slowing down (Fig. 14). The reason for this effect is complicated. The laminar flow is perturbed by the bumps and the perturbed flow is more resistant and permeable to separation. The local boundary layer entrains the freestream, and this seems to be the reason why the flow speedup is observed away behind the bumps.

With narrower roughness bumps in case AOA_4c.4n, the influence region of the high-speed flow is smaller than that in case

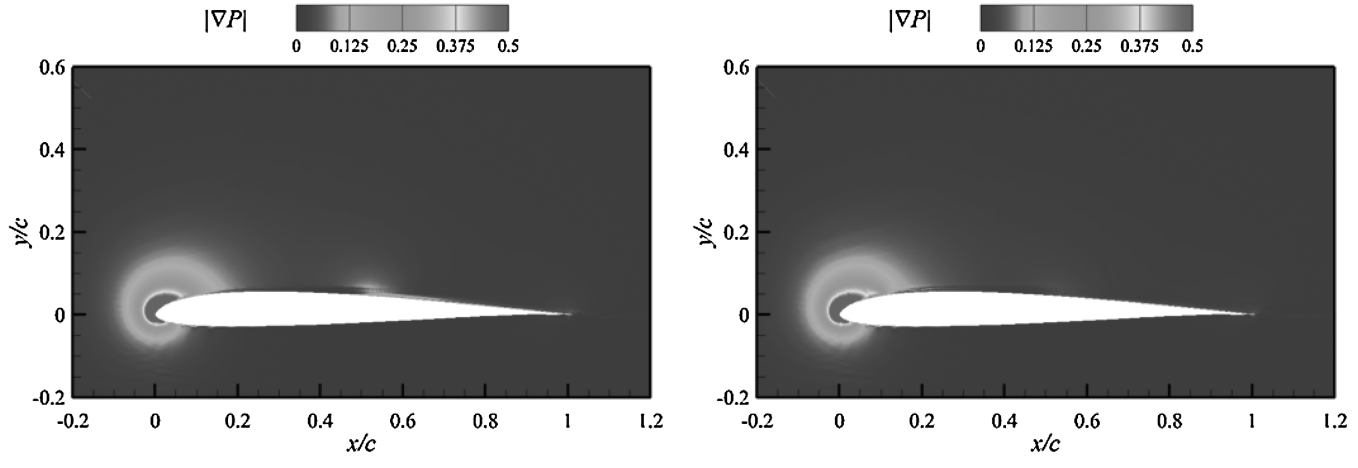

Fig. 12 Contours of pressure gradient magnitude. a) AOA_4c and b) AOA_4c.h.

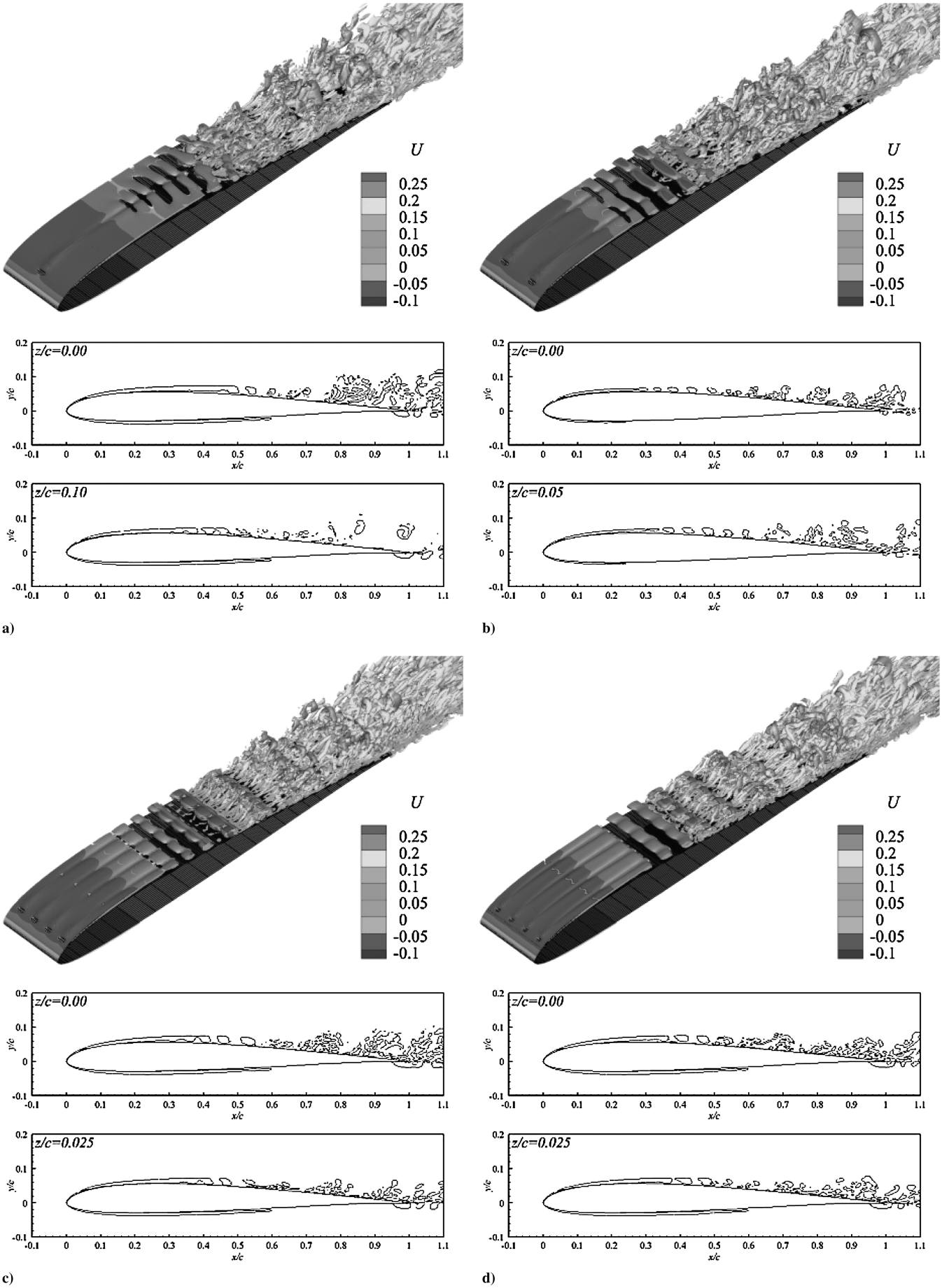

Fig. 13 Isosurface of Q-invariant colored by streamwise velocity and side view: a) AOA_4c.1, b) AOA_4c, c) AOA_4c.4, and d) AOA_4c.4n.

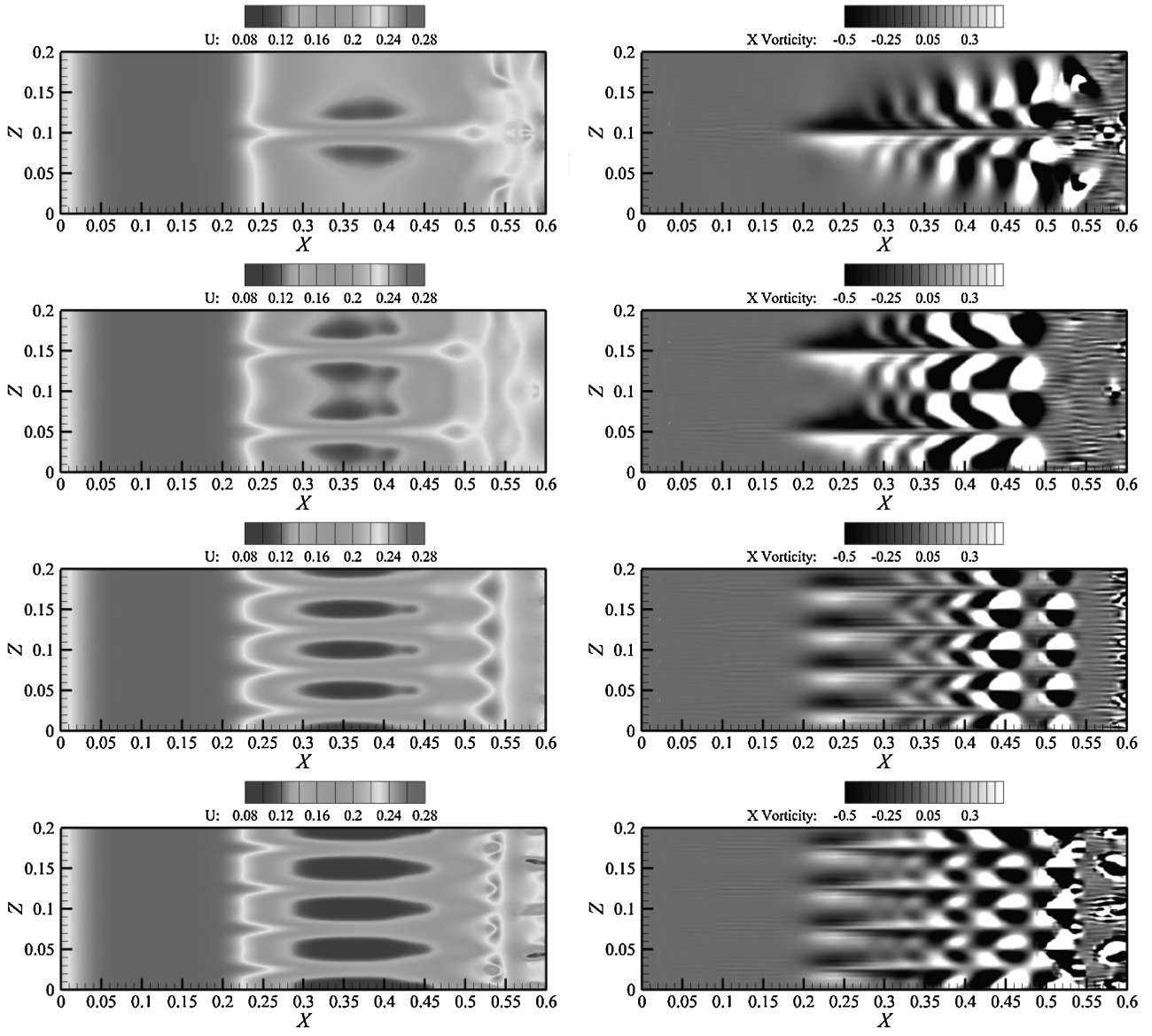

Fig. 14 Instantaneous contours of u velocity (left) and streamwise vorticity (right) on the sliced plane at $y = 0.065$; from top to bottom: AOA_4c.1, AOA_4c, AOA_4c.4, and AOA_4c.4n.

AOA_4c.4 (Fig. 14). The spanwise influences of the bumps on the laminar flowfield and the development of the streamwise vorticity in the separation region can be clearly seen in Fig. 14. The spanwise expansion of streamwise vorticities of case AOA_4c.1 is clearly shown in Fig. 14. With multiple roughness bumps over the span of the wings, the interaction between the streamwise vorticities generated by the adjacent bumps are shown in Fig. 14.

The mean pressure coefficient and friction coefficient distributions are shown in Fig. 15, in comparison with those of the baseline model AOA_4. The LSBs are reduced in all the cases with roughness bumps. The length of the LSB is longer for case AOA_4c.1 than that in case AOA_4c. However, further increasing the number of bumps N_{bump} does not further reduce the length of the LSBs. The mean pressure coefficient and friction coefficient distributions of cases AOA_4c.4 and AOA_4c.4n are found very close to those of AOA_4c (Fig. 15), and the separation region is even larger in case AOA_4c.4.

Table 5 presents the mean lift and drag coefficients per unit span and the lift-to-drag ratio of all the cases. With one roughness bump in case AOA_4c.1, both the drag coefficient and the pressure drag coefficient decrease. But the lift coefficient also decreases, such that only a little improvement of L/D ratio is achieved. Comparing between cases AOA_4c.1 and AOA_4c, the performance improvement has been achieved by increasing the number of bumps from one to two. With an equivalent volume of total bumps and similar behavior

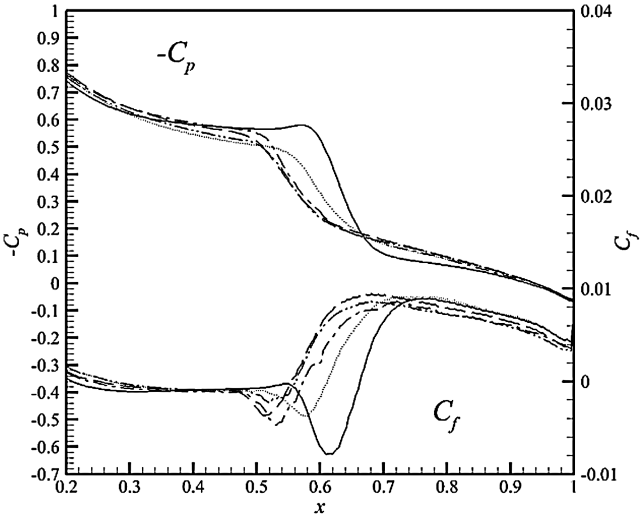

Fig. 15 Mean pressure coefficient and mean skin-friction coefficient on the wing surface; AOA_4 (solid line), AOA_4c.1 (dotted line), AOA_4c (dashed line), AOA_4c.4 (double-dot–dashed line) and AOA_4c.4n (dash-dotted line).

Table 5 Mean lift coefficient, drag coefficient (per unit span) and lift-to-drag ratio

Case	C_L	C_D	C_{Dp}	C_{Df}	L/D
AOA_4	0.600	2.34e − 2	1.38e − 2	0.97e − 2	25.6
AOA_4c.1	0.581	2.25e − 2	1.20e − 2	1.04e − 2	25.8
AOA_4c	0.593	2.05e − 2	1.00e − 2	1.05e − 2	28.9
AOA_4c.4	0.572	2.20e − 2	1.15e − 2	1.05e − 2	26.0
AOA_4c.4n	0.593	2.09e − 2	1.07e − 2	1.02e − 2	28.4

Table 6 Parameters of the roughness bumps for effects of the angle of attack

Case	X_E	W_{AC}	L_{BD}	H_{EF}	N_{bump}	δ_E	H_{EF}/δ_E
AOA_2c	0.05	0.045	0.045	0.0035	2	0.0046	76.1%
AOA_4c	0.05	0.045	0.045	0.0035	2	0.0049	71.4%
AOA_6c	0.05	0.045	0.045	0.0035	2	0.0056	62.5%

of the mean pressure and friction on the wall in cases AOA_4c and AOA_4c.4n, similar aerodynamic performance has achieved, as listed in Table 5. With four bumps in case AOA_4c.4 and twice the total bump volume as in case AOA_4c, the lift coefficient is degraded (5%) comparing with the baseline model. Although the drag coefficient is reduced due to the decrease of the pressure drag, the L/D ratio improvement is less than those in cases AOA_4c and AOA_4c.4n. This may imply that redundant bumps can be harmful to the aerodynamic performance.

C. Effects of the Angle of Attack

The effects of AOA are tested and investigated here by adjusting the incidence of the flow. AoA $= 2$ deg and 6 deg are considered and the same roughness configuration in case AOA_4c are used here. The geometric parameters of the roughness bumps in the cases of this section are shown in Table 6. At a different AOA, the boundary thickness δ_E is different, and the effects will be different. With the baseline model at different AOA, the thickness δ_E of the boundary layer and the ratio of the bump height H_{EF} to δ_E are listed in Table 6. Figure 16 shows the instantaneous isosurfaces and side views of Q-invariant of cases AOA_2 and AOA_2c, and Fig. 17 shows those of cases AOA_6 and AOA_6c. The mean pressure coefficient and friction coefficient distributions on the suction surface are shown in Fig. 18 for both AOA. The same results of cases AOA_4 and AOA_4c can be found Figs. 10 and 11. The LSBs are diminished in cases AOA_2c and avoided in case AOA_6c, as shown by the friction coefficient plots in Fig. 18. With the roughness bumps, the recovery of the pressure on the wall for all the controlled cases is much smoother than in the baseline model.

In case AOA_2c, the shedding vortices are found to be disturbed in a similar pattern as in case AOA_4c. In case AOA_6c, the periodic vortical packets are generated behind the bumps in the same pattern as in cases AOA_4c.h and AOA_4c.w. With the increase of AOA, the boundary-layer thickness δ_E at the bump location $X_E = 0.05$ increases (Table 6); thus, the ratio H_{EF}/δ_E decreases. It has been shown previously that at AoA $= 4$ deg and the same location, taller bumps with higher H_{EF}/δ_E ratio in case AOA_4c.h may generate larger disturbances and the vortical packets. However, here the situation is the opposite, and the vortical packets are generated behind the bumps in case AOA_6c with lower H_{EF}/δ_E ratio. This shows that the effects of the roughness bumps on the flowfield are not uniquely determined by the H_{EF}/δ_E ratio, but also by the instability features of the flowfield near the location of bumps. Figure 19a shows the mean tangential velocity profiles at location $x = 0.1$, which is right behind the location of the bumps $X_E = 0.05$, for the baseline model at three AOA. Figure 19b shows the wave speed s and growth rate α_i of the convective instability obtained by linear stability theory (LST) [47,48] based on the mean tangential velocity profiles, as

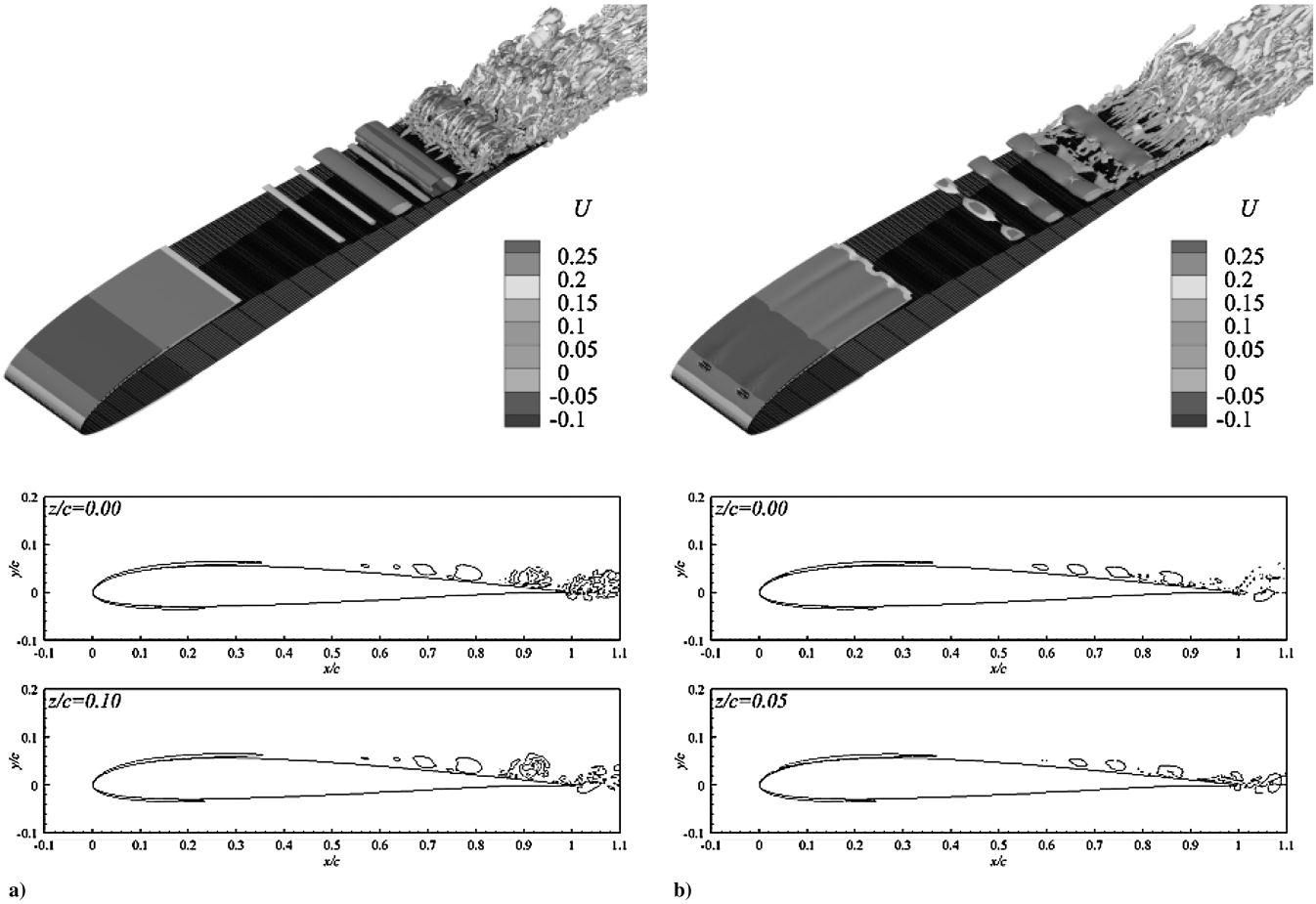

Fig. 16 Isosurface of Q-invariant colored by streamwise velocity at AOA $= 2$ deg: a) AOA-2 and b) AOA-2c.

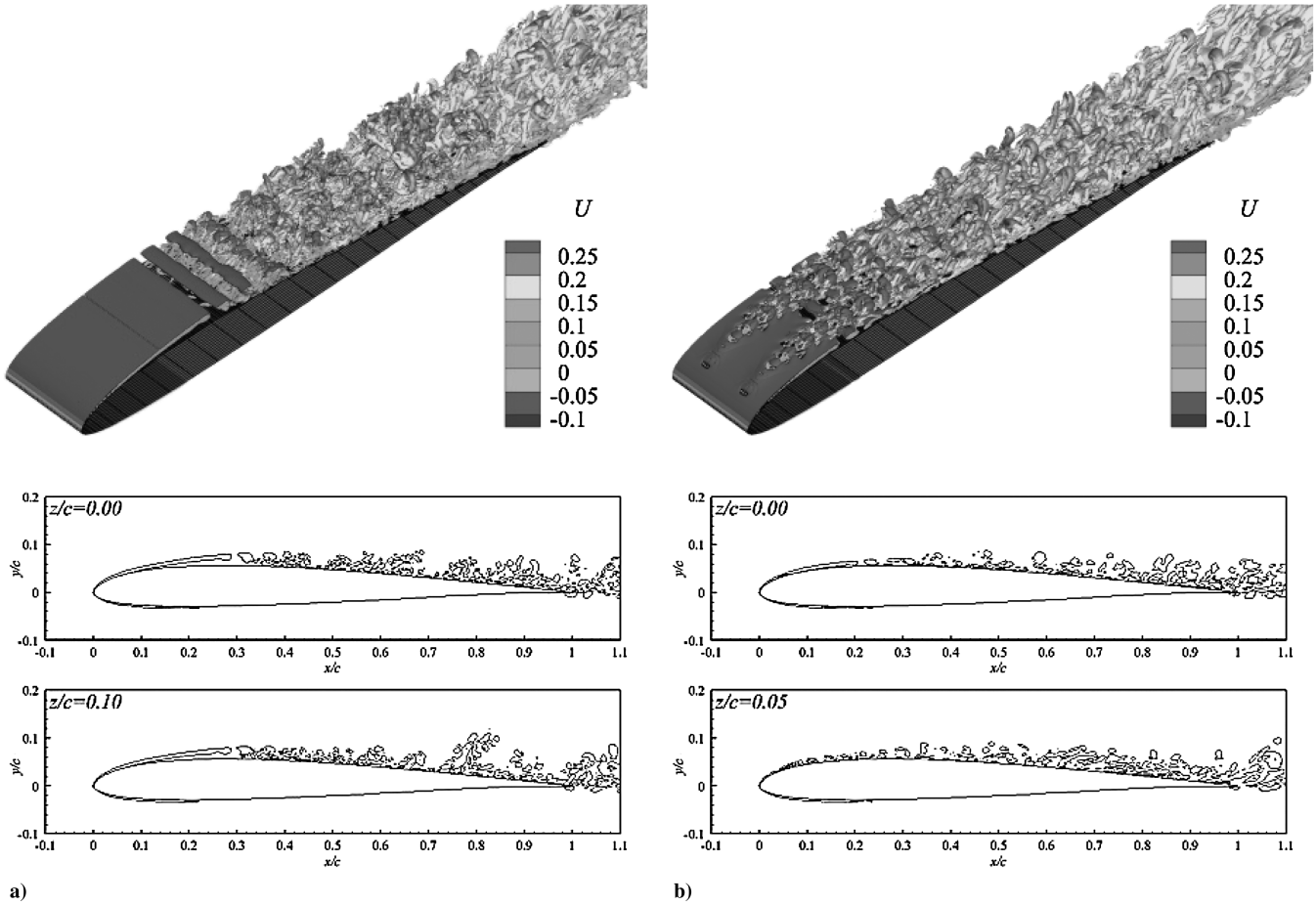

Fig. 17 Isosurface of Q-invariant colored by streamwise velocity at AOA = 6 deg: a) AOA_6 and b) AOA_6c.

shown in Fig. 19a. In LST, the fluctuations of the primitive variables $\phi = \{u, v, w, p, T, \rho\}$ are assumed to take the harmonic wave form: $\phi = \hat{\phi}(y)e^{i(\alpha x+\beta z-\omega t)}$. For convective instability (spatial instability), β and ω are assumed to be real and $\alpha = \alpha_r + i\alpha_i$ is complex. Thus, the flow is convective unstable if $\alpha_i < 0$, and vice versa. In case AOA_6c the location $x = 0.1$ is close to the mean separation point (Fig. 18) and the mean tangential velocity profile (Fig. 19a) generates the inflection point and separation. After separation, the K-H (inviscid) instability is usually more unstable and has a higher growth rate than the Tollmien–Schlitchting instability in the attached boundary layer. Both the unstable frequency range and the growth rate of the convective instability of AOA_6 are much larger than those in the other two cases (Fig. 19b). In cases AOA_2c and AOA_4c, the bumps locate further upstream from the mean separation points. The unstable frequency range and the growth rate of the convective instability of case AOA_4 are very small, as shown

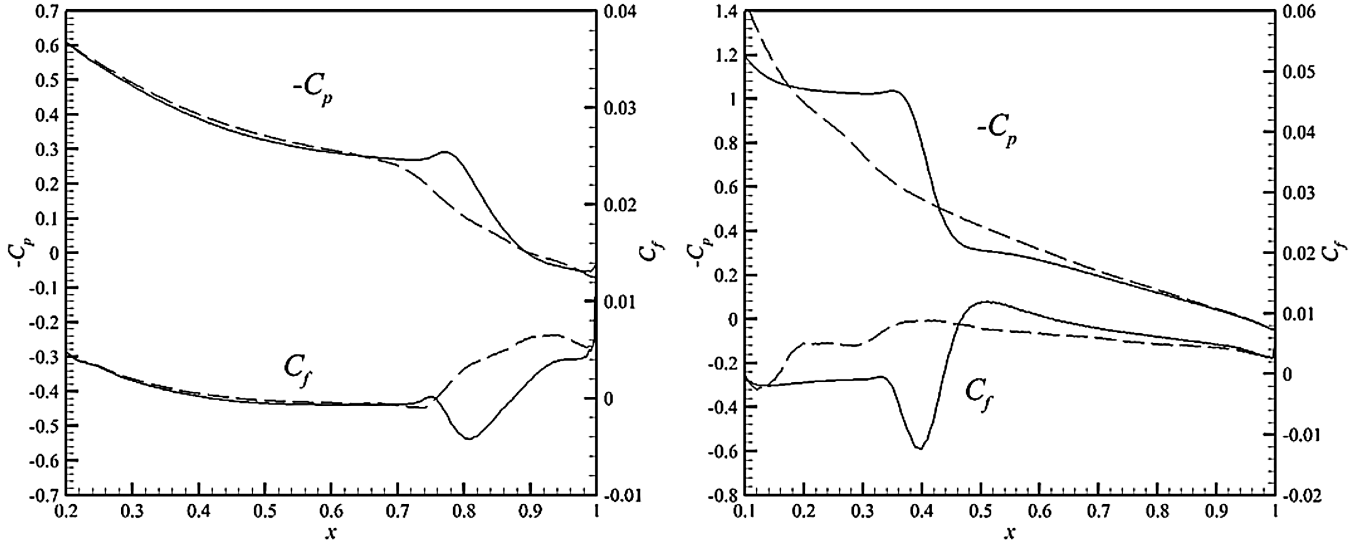

Fig. 18 Mean pressure coefficient and mean skin-friction coefficient on the wing surface; baseline model (solid line) and controlled case (dashed line): a) AOA = 2 deg and b) AOA = 6 deg.

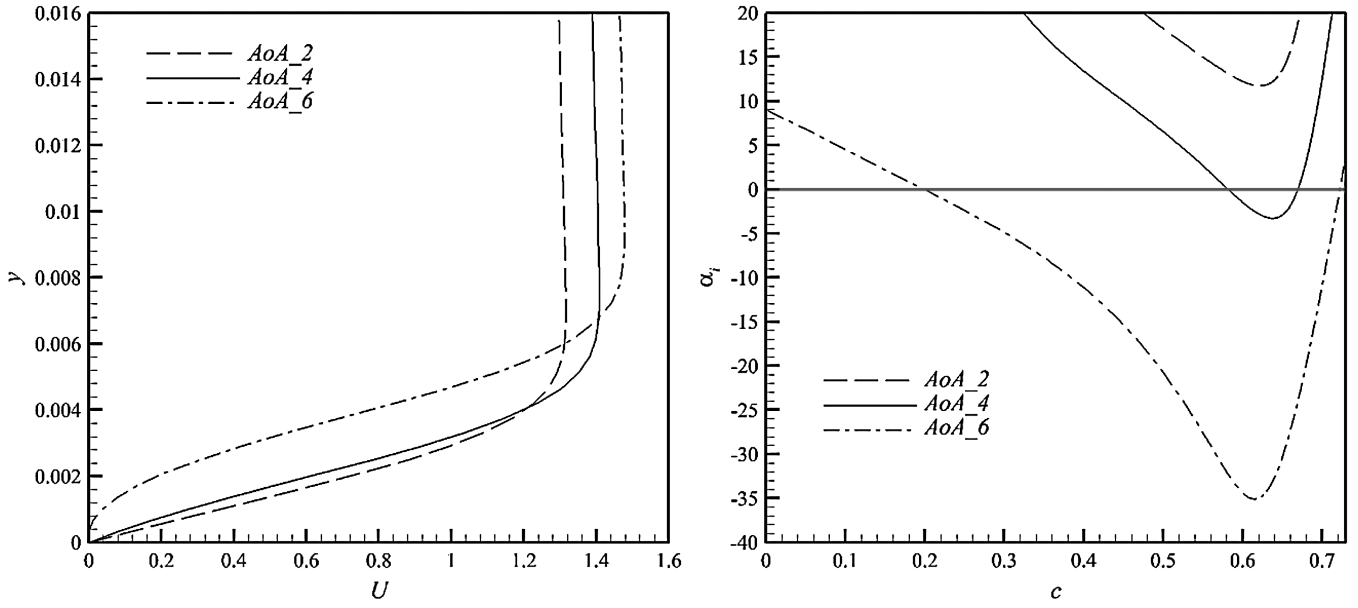

a) b)

Fig. 19 a) Tangential velocity profiles at $x = 0.1$ and b) unstable frequency range and growth rate of the convective instability obtained by LST at $x = 0.1$.

Table 7 Mean lift coefficient, drag coefficient (per unit span), and lift-to-drag ratio

Case	C_L	C_D	C_{Dp}	C_{Df}	L/D	Benefit
AOA-2	0.401	1.68e − 2	0.78-2	0.90e − 2	23.8	N/A
AOA-4	0.600	2.34e − 2	1.38e − 2	0.97e − 2	25.6	N/A
AOA-6	0.786	3.14e − 2	2.15e − 2	0.99e − 2	25.1	N/A
AOA-2c	0.400	1.63e − 2	0.68e − 2	0.95e − 2	24.5	3%
AOA-4c	0.593	2.05e − 2	1.00e − 2	1.05e − 2	28.9	13%
AOA-6c	0.766	2.56e − 2	1.37e − 2	1.19e − 2	29.9	19%

in Fig. 19b, and it is even convectively stable in case AOA_2 at location $x = 0.1$ as predicted by LST. Thus, the flow at $x = 0.1$ in case AOA_6c is more unstable to be perturbed by the bump and causes the generation of the vortical packets, although the H_{EF}/δ_E ratio is lower than these in cases AOA_2c and AOA_4c.

Table 7 lists the mean lift coefficient, drag coefficient, and lift-to-drag ratio for both the baseline and controlled cases at different AOA. In current cases, the roughness bumps are more effective on performance improvement at higher AOA. Figure 20 plots the pressure drag coefficient distributions and the lift-to-drag ratio for all the baseline and controlled cases at three AOA. In the baseline cases, the lift and drag both increase with the increase of the AOA (Table 7). However, the pressure drag force increases dramatically as the LSB moves upstream with the increase of AOA (Table 7 and Fig. 20b), which causes the deficit of the lift-to-drag ratio at AOA = 6 deg (Table 7 and Fig. 20a). In the controlled cases, the lift, the drag, and the pressure drag decreases at all the AOA, though the friction drag increases slightly because of the larger turbulent boundary-layer flow region. The L/D ratio is improved in the controlled cases at each of the AOA as listed in Table 7 and shown in Fig. 20. Especially for case AOA_6c, the L/D ratio increases significantly comparing with baseline case AOA_6 (Fig. 20a).

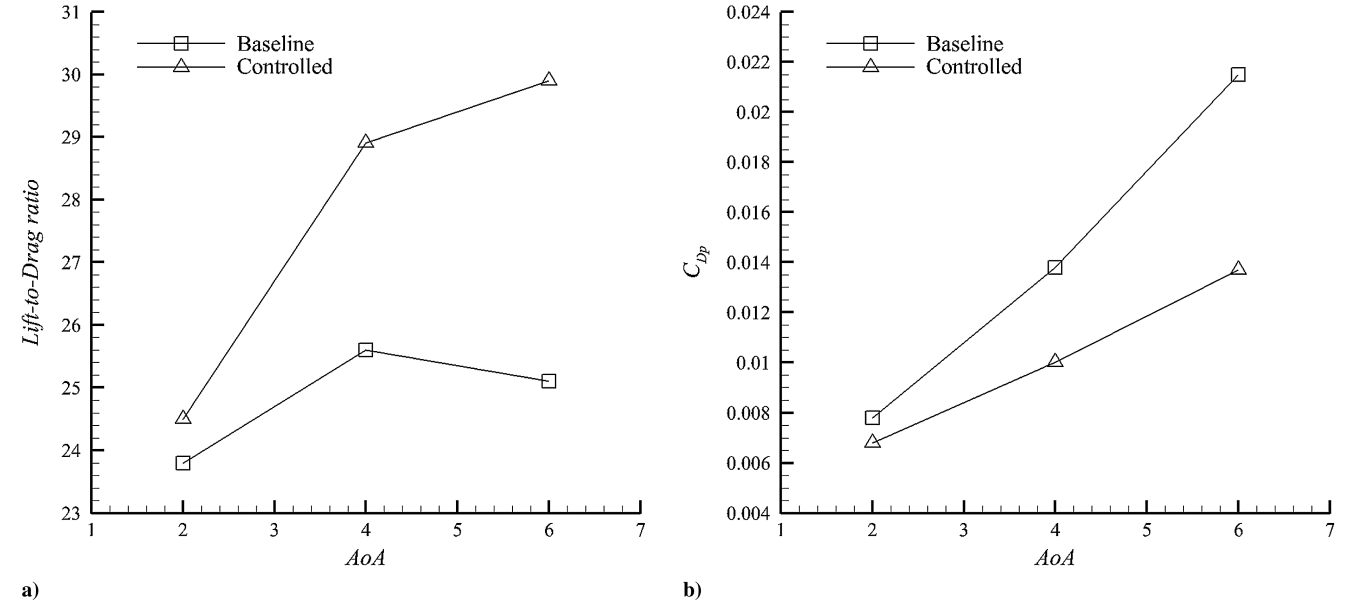

a) b)

Fig. 20 a) Lift-to-drag ratio and b) pressure drag coefficient distributions at different AOA.

V. Conclusions

The numerical simulations of a passive flow control technique using roughness bumps on a low-Reynolds-number wing are presented in this paper. A high-order spectral difference Navier–Stokes solver is used in the simulations. The SD method with unstructured hexahedral mesh is capable of capturing the separated flow and the transition process well over the suction side of the airfoil. The numerical results of the baseline cases and controlled cases are extensively investigated and discussed. The aerodynamic improvement using the current passive control is similar to the active mechanisms in the prior investigations. It is found that the aerodynamic improvement does not vary monotonically with the variations of the bump geometry and bump number.

By introducing the roughness bumps near the leading edge, the LSBs are reduced or avoided depending on the bump geometric parameters. It is found that larger and taller bumps generate larger disturbances, which trigger the vortex breakdown, and delay or avoid flow separation. In addition, the flow also transitions into turbulent flow sooner. Although the friction drag increases slightly, the pressure drag is significantly reduced resulting in an overall drag reduction. The reduction of LSBs by roughness bumps also slightly reduces the lift. However, the lift-to-drag ratio is increased in the cases with carefully chosen surface roughness bumps.

The effects of the surface roughness are also dependent on the number of roughness bumps. The aerodynamic performance is improved by increasing the number of bumps from one to two. However, the performance is degraded by further doubling the number of bumps. Reducing the width of the bumps by 50% regains the aerodynamic performance. The detailed physics are related with the three-dimensional K-H instability of the detached shear layer and, possibly, the elliptical instability of the shedding vortices, which is worth future investigation.

With a fixed configuration of bumps, the effects of bumps are tested over three AOA. It is found that the effects of roughness depend on multiple factors, including the size of the bumps and the instability of the local flow behind the roughness bumps. In the baseline cases, the LSB causes a dramatic increase of the pressure drag that decreases the lift-to-drag ratio with the increase of AOA. In the cases with surface roughness, the aerodynamic performance has been largely improved with the diminishing of the separated region, especially at higher AOA.

Acknowledgment

The authors would like to acknowledge the support from the U.S. Air Force Office of Scientific Research and the Department of Aerospace Engineering, Iowa State University.

References

[1] Galbraith, M., and Visbal, M., "Implicit Large Eddy Simulation of Low-Reynolds- Number Transitional Flow Past the SD7003 Airfoil, AIAA Paper 2010-737, Cincinnati, OH, 2010.

[2] Rizzetta, D. P., and Visbal, M. R., "Numerical Investigation of Plasma-Based Control for Low-Reynolds-Number Airfoil Flows," *AIAA Journal*, Vol. 49, No. 2, 2011, pp. 411–425. doi:10.2514/1.J050755

[3] Saric, W. S., Carrillo, R. B., Jr., and Reibert, M. S., "Leading-Edge Roughness as a Transition Control Mechanism," AIAA Paper 98-0781, 1998, 1998.

[4] Saric, W. S., and Reed, H. L., "Supersonic Laminar Flow Control on Swept Wings Using Distributed Roughness," AIAA Paper 2002-0147, 2002.

[5] White, E. B., and Saric, W. S., "Application of Variable Leading-Edge Roughness for Transition Control on Swept Wings," AIAA Paper 2000-0283, 2000.

[6] Carpenter, A. L., Saric, W. S., and Reed, H. L., "In-Flight Receptivity Experiments on a 30-Degree Swept-Wing Using Micron-Sized Discrete Roughness Elements," AIAA Paper 2009-590, Jan. 2009.

[7] Carpenter, A. L., Saric, W. S., and Reed, H. L., "Roughness Receptivity in Swept-Wing Boundary Layers—Experiments," *International Journal of Engineering Systems Modelling and Simulation*, Vol. 2, Nos. 1/2, Mar. 2010, pp. 128–138. doi:10.1504/IJESMS.2010.031877

[8] Ergin, F. G., and White, E. B., "Unsteady and Transitional Flows Behind Roughness Elements," *AIAA Journal*, Vol. 44, No. 11, 2006, pp. 2504–2514. doi:10.2514/1.17459

[9] Berg, D., "Surface Roughness Effect on a Mach 6 Turbulent Boundary Layer," *AIAA Journal*, Vol. 17, No. 9, 1979, pp. 929–930. doi:10.2514/3.61254

[10] Latin, R., and Bowersox, R., "Temporal Turbulent Flow Structure for Supersonic Rough-Wall Boundary Layers," *AIAA Journal*, Vol. 40, No. 5, 2002, pp. 832–841. doi:10.2514/2.1749

[11] Fransson, J. H. M., Talamelli, A., Brandt, L., and Cossu, C., "Delaying Transition to Turbulence by a Passive Mechanism," *Physical Review Letters*, Vol. 96, 2006, p. 064501. doi:10.1103/PhysRevLett.96.064501

[12] Fransson, J. H. M., Brandt, L., Talamelli, A., and Cossu, C., "Experimental and Theoretical Study of the Stabilization of Tollmien–Schlichting Waves by Finite Amplitude Streaks," *Physics of Fluids*, Vol. 17, 2005, Paper 054110. doi:10.1063/1.1897377

[13] Zhang, Y., Igarashi, T., and Hu, H., "Experimental Investigations on the Performance Degradation of a Low-Reynolds-Number Airfoil with Distributed Leading Edge Roughness," AIAA Paper 2011-1102, 2011.

[14] Honsaker, R., and Huebsch, W. W., "Parametric Study of Dynamic Surface Roughness as a Mechanism for Flow Control," AIAA Paper 2005-4732, 2005.

[15] Rizzetta, D. P., and Visbal, M. R., "Direct Numerical Simulation of FlowPast an Array of Distributed Roughness Elements," *AIAA Journal*, Vol. 45, No. 8, Aug. 2007, pp. 1967–1976. doi:10.2514/1.25916

[16] Rizzetta, D., Visbal, M., Reed, H., and Saric, W., "Direct Numerical Simulation of Discrete Roughness on a Swept-Wing Leading Edge," *AIAA Journal*, Vol. 48, No. 11, 2010, pp. 2660–2673. doi:10.2514/1.J050548

[17] Redford, J., Sandham, N., and Roberts, G., "Compressibility Effects on Boundary-Layer Transition Induced by an Isolated Roughness Element," *AIAA Journal*, Vol. 48, No. 12, 2010, pp. 2818–2830. doi:10.2514/1.J050186

[18] Santhanakrishnan, A., and Jacob, J. D., "Effect of Regular Surface Perturbations on Flow over an Airfoil," AIAA Paper 2005-5145, 2005.

[19] Boiko, A. V., Dovgal, A. V., and Hein, S., "Control of a Laminar Separating Boundary Layer by Induced Stationary Perturbations," *European Journal of Mechanics, B/Fluids*, Vol. 27, Issue 4, July–Aug. 2008, pp. 466–476. doi:10.1016/j.euromechflu.2007.09.005

[20] Patera, A. T., "A Spectral Element Method for Fluid Dynamics: Laminar Flow in a Channel Expansion," *Journal of Computational Physics*, Vol. 54, 1984, p. 468. doi:10.1016/0021-9991(84)90128-1

[21] Kopriva, D. A., and Kolias, J. H., "A Conservative Staggered-Grid Chebyshev Multidomain Method for Compressible Flows," *Journal of Computational Physics*, Vol. 125, 1996, p. 244. doi:10.1006/jcph.1996.0091

[22] Kopriva, D. A., and Kolias, J. H., "A Staggered-Grid Multidomain Spectral Mthod for the Compressible Navier–Stokes Equations," *Journal of Computational Physics*, Vol. 143, 1998, pp. 125–158. doi:10.1006/jcph.1998.5956

[23] Barth, T. J., and Frederickson, P. O., "High-Order Solution of the Euler Equations on Unstructured Grids using Quadratic Reconstruction," AIAA Paper No. 90-0013, 1990.

[24] Hu, C., and Shu, C.-W., "Weighted Essentially Nonoscillatory Schemes on Triangular Meshes," *Journal of Computational Physics*, Vol. 150, 1999, p. 97. doi:10.1006/jcph.1998.6165

[25] Cockburn, B., and Shu, C.-W., "TVB Runge-Kutta Local Projection Discontinuous Galerkin Finite Element Method for Conservation Laws II: General Framework," *Mathematics of Computation*, Vol. 52, 1989, p. 411.

[26] Abgrall, R., and Roe, P. L., "High Order Fluctuation Schemes on Triangular Meshes," *Journal of Scientific Computing*, Vol. 19, 2003, pp. 3–36. doi:10.1023/A:1025335421202

[27] Wang, Z. J., and Liu, Y., "Spectral (Finite) Volume Method for Conservation Laws on Unstructured Grids III: Extension to One-Dimensional Systems," *Journal of Scientific Computing*, Vol. 20, No. 1, 2004, pp. 137–157. doi:10.1023/A:1025896119548

[28] Liu, Y., Vinokur, M., and Wang, Z. J., "Discontinuous Spectral Difference Method for Conservation Laws on Unstructured Grids," *3rd International Conference in CFD*, Toronto, July 2004.
[29] Liu, Y., Vinokur, M., and Wang, Z. J., "Multi-Dimensional Spectral Difference Method for Unstructured Grids," AIAA Paper 2005-0320, 2005.
[30] Wang, Z. J., and Liu, Y., "The Spectral Difference Method for the 2-D Euler Equations on Unstructured Grids," AIAA Paper 2005-5112, 2005.
[31] Huang, P. G., Wang, Z. J., and Liu, Y., "An Implicit Space-Time Spectral Difference Method for Discontinuity Capturing Using Adaptive Polynomials," AIAA Paper 2005-5255, 2005.
[32] Sun, Y., Wang, Z. J., and Liu, Y., "High-Order Multidomain Spectral Difference Method for the Navier–Stokes Equations on Unstructured Hexahedral Grids," *Communications in Computational Physics*, Vol. 2, No. 2, 2007, pp. 310–333.
[33] Zhou, Y., and Wang, Z. J., "Implicit Large Eddy Simulation of Transitional Flow over a SD7003 Wing Using High-Order Spectral Difference Method," AIAA Paper 2010-4442.
[34] Roe, P. L., "Approximate Riemann Solvers, Parameter Vectors, and Difference Schemes," *Journal of Computational Physics*, Vol. 43, 1981, pp. 357–372.
doi:10.1016/0021-9991(81)90128-5
[35] Galbraith, M., and Visbal, M., "Implicit Large Eddy Simulation of Low Reynolds Number Flow Past the SD7003 Airfoil," 46th AIAA Aerospace Sciences Meeting and Exhibit, AIAA Paper 2008-225, Reno, NV, 2008.
[36] Ol, M. V., Hanff, E., McAuliffe, B., Scholz, U., and Kaehler, C., "Comparison of Laminar Separation Bubble Measurements on a Low Reynolds Number Airfoil in Three Facilities," 35th AIAA Fluid Dynamics Conference and Exhibit, AIAA Paper 2005-5149, Toronto, June 6–9 2005.
[37] Zhou, Y., and Wang, Z. J., "Absorbing Boundary Conditions for the Euler and Navier–Stokes Equations with the Spectral Difference Method," *Journal of Computational Physics*, Vol. 229, 2010, pp. 8733–8749.
doi:10.1016/j.jcp.2010.08.007
[38] Volino, R. J., and Hultgren, L. S., "Measurements in Separated and Transitional Boundary Layers Under Low-Pressure Turbine Airfoil Conditions," *Journal of Turbomachinery*, 123, 2001, pp. 189–197.
doi:10.1115/1.1350408
[39] Burgmann, S., Brucker, S., and Schroder, W., "Scanning PIV Measurements of a Laminar Separation Bubble," *Experiments in Fluids*, Vol. 41, 2006, pp. 319–326.
doi:10.1007/s00348-006-0153-6
[40] Hu, H., and Yang, Z. F., "An Experimental Study of the Laminar Flow Separation on a Low-Reynolds-Number Airfoil," *Journal of Fluids Engineering*, Vol. 130, May 2008, Paper 051101.
doi:10.1115/1.2907416
[41] Dubeif, Y., and Delcayre, F., "On Coherent-Vortex Identification in Turbulence," *Journal of Turbulence*, Vol. 1, No. 1, 2000, pp. 1–22.
10.1088/1468-5248/1/1/011doi:
[42] Spalart, P. R., and Strelets, M. K. H., "Mechanisms of Transition and Heat Transfer in a Separation Bubble," *Journal of Fluid Mechanics*, Vol. 403, 2000, pp. 329–349.
doi:10.1017/S0022112099007077
[43] Jones, L. E., Sandberg, R. S., and Sandham, N. D., "Direct Numerical Simulations of Forced and Unforced Separation Bubbles on an Airfoil at Incidence," *Journal of Fluid Mechanics*, Vol. 602, 2008, pp. 175–207.
[44] Fasel, H. F., Balzer, W., and Gross. A., "Investigation of Separation Control for Low-Pressure Turbines Using CFD," *26th International Congress of the Aeronautical Sciences*, 2008.
[45] Zaki, T. A., Wissink, J. G., Rodi W., and Durbin, P. A., "Direct Numerical Simulations of Transition in a Compressor Cascade: The Influence of Free-Stream Turbulence," *Journal of Fluid Mechanics*, Vol. 665, 2010, pp. 57–98.
doi:10.1017/S0022112010003873
[46] Williamson, C. H. K., "Three-Dimensional Wake Transition," *Journal of Fluid Mechanics*, Vol. 328, 1996, pp. 345–407.
doi:10.1017/S0022112096008750
[47] Drazin, P. G., *Introduction to Hydrodynamic Stability*, Cambridge University Press, New York, 2002.
[48] Malik, M. R., "Numerical Methods for Hypersonic Boundary Layer Stability," *Journal of Computational Physics*, Vol. 86, 1990, pp. 376–413.
doi:10.1016/0021-9991(90)90106-B

S. Fu
Associate Editor